JGR Solid Earth

RESEARCH ARTICLE
10.1029/2022JB026278

Joint Inversion of Geodetic and Strong Motion Data for the 2012, M_w 6.1–6.0, May 20th and May 29th, Northern Italy Earthquakes: Source Models and Seismotectonic Interpretation

L. Improta[1], A. Cirella[2], G. Pezzo[1], I. Molinari[3], and A. Piatanesi[1]

[1]Istituto Nazionale di Geofisica e Vulcanologia, Osservatorio Nazionale Terremoti, Roma, Italy, [2]Istituto Nazionale di Geofisica e Vulcanologia, Sezione Sismologia e Tettonofisica, Roma, Italy, [3]Istituto Nazionale di Geofisica e Vulcanologia, Bologna, Italy

Key Points:

- Rupture models of the 2012 northern Italy mainshocks obtained by inverting the most comprehensive geodetic and strong motion data set to date
- Both mainshocks ruptured two asperities along moderately dipping thrusts rooted into the Paleozoic crystalline basement down to ~15 km depth
- Asperities located in Mesozoic carbonates and Paleozoic basement and slip distribution controlled by lithological and structural barriers

Supporting Information:

Supporting Information may be found in the online version of this article.

Correspondence to:

A. Cirella,
antonella.cirella@ingv.it

Citation:

Improta, L., Cirella, A., Pezzo, G., Molinari, I., & Piatanesi, A. (2023). Joint inversion of geodetic and strong motion data for the 2012, M_w 6.1–6.0, May 20th and May 29th, northern Italy earthquakes: Source models and seismotectonic interpretation. *Journal of Geophysical Research: Solid Earth*, *128*, e2022JB026278. https://doi.org/10.1029/2022JB026278

Received 16 DEC 2022
Accepted 27 APR 2023

Author Contributions:

Conceptualization: L. Improta, A. Cirella
Data curation: L. Improta, A. Cirella, G. Pezzo
Formal analysis: L. Improta, A. Cirella, I. Molinari
Investigation: L. Improta, A. Cirella, G. Pezzo, I. Molinari, A. Piatanesi
Methodology: L. Improta, A. Cirella
Writing – original draft: L. Improta, A. Cirella

Abstract We present the first rupture models of the two mainshocks of the 2012 northern Italy sequence, determined by jointly inverting seismic and geodetic data. We aim at providing new insights into the mainshocks for which contrasting seismotectonic interpretations are proposed in literature. Sources' geometric parameters were constrained by seismic reflection profiles, 3-D relocations and focal mechanisms of mainshocks/aftershocks. Site-specific velocity profiles were used to model accelerograms affected by strong propagation effects related to the Po basin. Our source models differ significantly from previous ones relying on either seismic or geodetic data. Their comparison against geological sections and aftershock distribution provides new insights about the ruptured thrust faults. The May 20th M_w6.1 mainshock activated the Middle Ferrara thrust-ramp dipping ~45° SSW-wards, breaking a main eastern slip patch 4–15 km deep in Mesozoic carbonates (maximum slip 0.7–0.8 m) and Paleozoic-Triassic basement rocks, and a small western patch in the basement. The May 29th M_w6.0 mainshock featured two separated asperities along the Mirandola thrust-ramp dipping ~42° S-wards: an eastern asperity 4–15 km deep in Mesozoic carbonates and basement rocks (maximum slip 0.7 m) and a deeper western one (7–16 km depth) mainly in the basement (slip peak 0.8 m). On-fault aftershocks were concentrated within the basement and Mesozoic carbonates, devoiding high-slip zones. Slip and aftershock distribution was controlled by the rheological transition between Mesozoic carbonates and Cenozoic sediments. Unlike previous thin-skinned tectonic interpretations, our results point to a complex rupture process along moderately dipping (40°–45°) thrust-ramps deeply rooted into the Paleozoic crystalline basement.

Plain Language Summary The two M6 mainshocks of the 2012 Italy sequence are the strongest earthquakes ever observed in the Po Plain, a strategic region for the Italian economy. The mainshocks ruptured blind thrust-faults, however their source models and seismotectonic interpretation are still debated because the thrust-system architecture is controversial. Contrasting thick-skinned and thin-skinned tectonic models are proposed. In thick-skinned interpretations, shortening is accommodated by thrust-ramps rooted into the crystalline basement that represent main seismogenic structures, whereas in thin-skinned interpretations, shortening and seismicity are controlled by listric faults splaying out from dècollement levels in the sedimentary crust. A comprehensive analysis of the mainshocks' source represents an opportunity to provide new insights into the seismogenesis in northern Italy and on a broader scale into seismotectonics of thrust-and-fold belts. We get a complete picture of the mainshocks kinematics by jointly inverting, for the first time, seismic and geodetic data, and unravel rupture heterogeneities not resolved by previous studies. By integrating source models with aftershock locations and geological models, we propose a comprehensive seismotectonic interpretation of the sequence. We conclusively identify the ruptured faults that correspond to thrust-ramps rooted into the crystalline basement and evidence the key role played by lithological changes in the rupture process.

1. Introduction

In May and June 2012, a seismic sequence struck the Po Plain sedimentary basin (Emilia region, northern Italy) (Figure 1a). Two thrust-faulting mainshocks occurred on May 20th and May 29th with estimated M_w of 6.1 and 5.9, respectively (Pondrelli et al., 2012). The seismic sequence, that includes six $M_L > 5$ aftershocks, hit an area

Writing – review & editing: L. Improta, A. Cirella, G. Pezzo, I. Molinari, A. Piatanesi

characterized by moderate seismicity where earthquakes of M6+ have neither been reported in the historical catalogs over the last 1,000 years (Figure 1a; Rovida et al., 2011). Thus, the May 20th and May 29th mainshocks are the largest earthquakes ever instrumentally recorded in the Po Plain.

The epicentral region is located in the outer zone of the northern Apennines, a Neogene-Quaternary thrust-and-fold belt (Figure 1a). The seismic sequence activated thrust faults buried underneath the Po Plain Plio-Quaternary basin (Bonini et al., 2014, among others). These faults belong to a WNW-ESE trending and S-dipping complex thrust-and-fold system that consists of two main structures: the Ferrara Thrust System to the north and the arcuate Mirandola Thrust System located in a more internal and western position (Figures 1a and 1b).

The Po Plain sedimentary basin has been deeply explored by the hydrocarbon industry since the 60s (Pieri & Groppi, 1981). More authors compared subsurface geological models with seismological data (Astiz et al., 2014; Bonini et al., 2014; Carannante et al., 2015; Chiarabba et al., 2014; Govoni et al., 2014; Juanes et al., 2016; Lavecchia et al., 2015; Malagnini et al., 2012), or with source models determined by geodetic data inversion (Cheloni et al., 2016; Pezzo et al., 2018) coming up with seismotectonic interpretations of the seismic sequence. However, very different interpretations have been proposed and the geometry of the mainshocks faults is still debated (see Argnani et al. (2016) for a review). This strictly relates to major unsolved questions that remain regarding the internal architecture of the thrust systems and the overall structural style. Indeed, contrasting thick-skinned, thin-skinned and mixed-thin-thick-skinned tectonic models have been proposed in literature (Fantoni & Franciosi, 2010; Livani et al., 2018; Turrini et al., 2014, among others). In thick-skinned tectonic interpretations, the dominant structural style is that of ramp-dominated thrusting, with moderate- to high-angle thrust faults deeply rooted into the crystalline basement (Juanes et al., 2016). Whereas in thin-skinned interpretations, the dominant style is that of detachment-dominated thrusting with low-angle and listric faults splaying out from relatively shallow dècollement levels in the sedimentary crust (Carminati et al., 2010). The Po Plain is densely populated, hosts key industrial districts and represents a strategic region for the Italian economy. Despite their moderate magnitude, the mainshocks caused 27 casualties and an economic loss of 13 billion Euros (i.e., about 1% of gross national product) because of extensive collapses and damages. This dramatic impact reflected the high vulnerability of most residential buildings and industrial facilities and widespread ground motion amplification effects (Bordoni et al., 2012). Consequently, the 2012 events renewed the interest among geoscientists for seismic hazard assessment of that wide sector of the Po Plain that extends above the buried active fronts of the Apennines.

The May 20th and May 29th mainshocks are the first relevant earthquakes recorded by a wide range of instruments in northern Italy (broadband seismic sensors, accelerometer, satellite SAR, GPS, and high frequency GPS), offering, for the first time, the opportunity to constrain the rupture process of large thrust faulting earthquakes with different types of data. Moreover, in our cross-disciplinary study, we integrated hydrocarbon exploration data and accurate aftershock locations which allowed us to better determine the finite-fault source models and to provide a comprehensive seismotectonic interpretation of the seismic sequence.

We imaged the rupture process of the two mainshocks by jointly inverting strong motion recordings, high-rate continuous GPS data (HRGPS), GPS and Differential Interferometry Synthetic Aperture Radar (DInSAR) displacements. With respect to previous works (Causse et al., 2017; Cheloni et al., 2016; Convertito et al., 2021; Ganas et al., 2012; Nespoli et al., 2017; Pezzo et al., 2013, 2018), we produced the first rupture models that honor both strong motion and geodetic data. In addition, we used for the first time strong motion stations installed by Istituto Nazionale di Geofisica e Vulcanologia (INGV) soon after the May 20th mainshock (Re.Mo. network; Moretti et al., 2012).

We remark that kinematic inversion of strong motion recordings for the 2012 Emilia mainshocks is a challenging task. Marked heterogeneities in the upper crustal velocity structure (Chiarabba et al., 2014) cause complex propagation effects evidenced by strong ground motion amplifications (Bordoni et al., 2012). To tackle these difficulties and to separate adequately source and propagation effects, we used site-specific calibrated Green Functions (GFs) by using a 3-D regional crustal model of the Po Plain basin (Molinari et al., 2015).

We performed earthquake source model inversions by testing different planar faults whose geometrical parameters are constrained by seismic reflection and well data, published subsurface structural models (Astiz

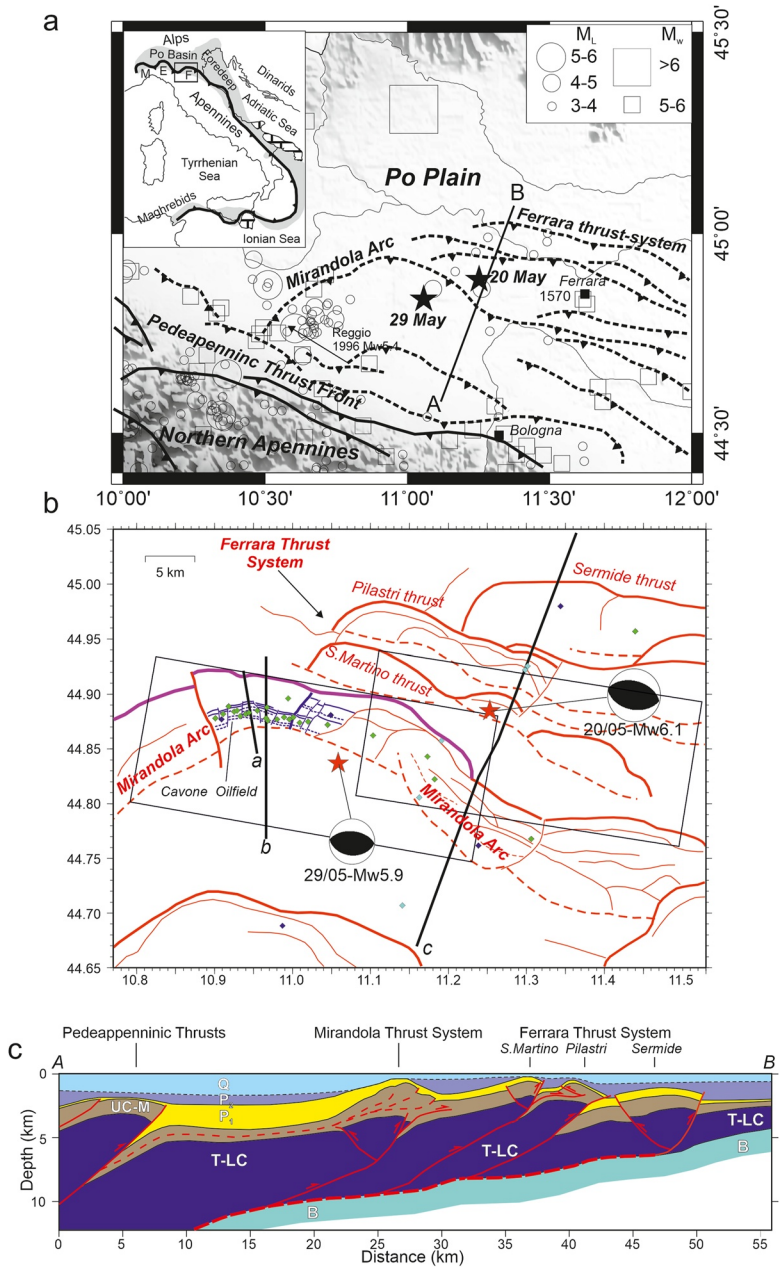

Figure 1. (a) Structural sketch of the northern Apennines and western Ferrara-Romagna arc. Historical and instrumental seismicity (April 1990 - January 2012) is shown with squares and circles, respectively, of size proportional to the magnitude. The stars depict the two 2012 mainshocks. The 1,570, M_w5.5 Ferrara earthquakes, that is the closest historical event, is highlighted in the map. The thick black line is the trace of the geological section shown in panel (c). The dashed lines represent buried thrust fronts. The inset map shows the central Mediterranean region. The thick black line is the outer front of the Apennines; labels evidence the northern Apennines buried arcs (M—Monferrato, E—Emilia, F—Ferrara Romagna arc). (b) Structural map of the Mirandola and Ferrara thrust systems with outlined Plio-Quaternary reverse faults (modified from Bigi et al., 1991). Thick red lines are the main thrust fronts of the Mirandola Arc and of the Inner, Middle and Outer Ferrara thrust systems (San Martino, Pilastri and Sermide structures, respectively), dashed red lines back-thrusts, thin red lines minor compressive structures. The thick magenta line corresponds to the tip of the Mirandola frontal thrust reported by Astiz et al. (2014). The main thrusts, back-thrusts and transpressive faults cutting the carbonate reservoir in the Cavone oilfield are shown with blue lines (modified from Nardon et al., 1991). Small diamonds are wells analyzed in this study: green—wells reaching the Mesozoic carbonates, cyan—well penetrating Cenozoic sequences, blue—deep wells with sonic logs. Interpreted sonic logs are from wells: Cavone 1 and Concordia 1 (reported by Styles et al., 2014), Sermide 1, Bevilacqua 1, Case Pinelli 1, Cascina Nuova 1 (from ViDEPI Project, 2015). Beach-balls denote the TDMT mechanisms of the two mainshocks (Scognamiglio et al., 2012, 2016). The thick black lines correspond to the seismic profiles shown in Figure 5 (profile *c*) and 6 (profile *a*), and to the geological section shown in Figure 12 (trace *b*). The two rectangles represent the two best-fit planar faults of the finite-fault inversion. (c) Schematic geological section across the Mirandola and Ferrara thrust systems (modified from Carminati et al., 2010): Q—Quaternary marine and continental deposits, P2—Upper Pliocene terrigenous sequences, P1—Lower-Middle Pliocene terrigenous sequences, UC-M—Upper Cretaceous to Miocene carbonates, marls and terrigenous sequences, TI-C—Lower Triassic to Cretaceous evaporites, shelf limestones and carbonate condensed successions, B—Paleozoic basement s.l.

et al., 2014; Bencini, 2009), 3D locations and source mechanisms of the aftershocks and mainshocks (Chiarabba et al., 2014; Malagnini et al., 2012; Scognamiglio et al., 2012, 2016).

Our first goal is to reconstruct the rupture history of both earthquakes. Then, we compared the obtained source models with interpreted seismic profiles and aftershock distribution to: (a) pinpoint the thrust faults ruptured by the mainshocks, (b) investigate the relation between rock lithology, slip distribution and aftershocks, (c) propose an updated seismotectonic interpretation of the seismic sequence.

2. Geological and Seismotectonic Setting

The 2012 seismic sequence occurred in the outer portion of the northern Apennines, a NE-verging thrust-and-fold belt originated since Oligocene by the subduction of the Adria microplate under Eurasia (Figure 1a) (Doglioni et al., 1999; Royden et al., 1987). In the outer frontal portion of the belt, blind thrust systems define three main arcs buried under the Po Plain foreland basin: from west to east, the Monferrato, the Emilia, and the Ferrara-Romagna arcs (Pieri & Groppi, 1981). The seismic sequence activated structures belonging to the western Ferrara-Romagna arc that is in turn structured in two thrust-fold systems: the WNW-ESE striking Ferrara Thrust System to the north and the arcuate Mirandola Thrust System to the southwest (Figures 1a–1c). Shortening in this outer portion of the belt initiated in the Late Messinian and migrated forelandward (Livani et al., 2018; Maesano et al., 2015). Meso-Cenozoic sedimentary sequences of Adria were progressively incorporated in the thrust-belt that overthrust the foreland regional monocline gently dipping southwestward. The regional subsidence caused by the flexure of the subducting Adria was faster than the uplift of local thrust-related anticlines (Carminati & Martinelli, 2002). Consequently, huge syntectonic wedges of Plio-Pleistocene sediments deposited in synclines separated by shallow thrust-related anticlines (Carminati et al., 2010; Pieri & Groppi, 1981; Turrini et al., 2014) (Figure 1c).

The deep part of the sedimentary succession is formed by shallow-to-deep water carbonates (Upper Triassic dolomites, Jurassic limestones) followed by Lower Cretaceous marls and Upper Cretaceous - Lower Eocene pelagic limestones and carbonate resediments (Styles et al., 2014; Livani et al., 2018 among others). This carbonate multilayer has thickness ranging between 2.5 and 4 km and covers a basement *sensu lato* (s.l.) composed of Middle Triassic - Permian evaporites, siliciclastic deposits, volcanites and metasediments, as proposed by Bonini et al. (2014) on the basis of seismic facies of deep reflection profiles crossing the western Ferrara-Romagna Arc. Their interpretation is coherent with deep wells in the northern Adriatic Sea (ViDEPI Project, 2015) that penetrated these Triassic–Permian rocks above lower Paleozoic granitoids of the Hercynian crystalline basement (Fantoni & Franciosi, 2010; Patacca et al., 2008).

The upper part of the sedimentary sequence consists mainly of Middle Eocene - Miocene marls, marly limestones and siliciclastic deposits (Figure 1c) (Livani et al., 2018; Styles et al., 2014). The Lower Pliocene record includes transgressive siliciclastic turbidites showing significant thickness variations. In the Middle-Late Pliocene the sedimentation was controlled by contractional tectonics (Carminati et al., 2010; Turrini et al., 2014). Terrigenous turbidites formed up to 7-km-thick sequences in deep synclines, or, alternatively, thin covers above the growing anticlines (Figure 1c). The siliciclastic supply went on during the Pleistocene when marine sands deposited also above the anticlines following a regional subsidence. The shallower sediments are Late Pleistocene-Holocene fluvio-lacustrine deposits.

The internal architecture of the Mirandola and Ferrara arcs is still debated (see Argnani et al., 2016 and references therein). Main controversial issues are the overall tectonic style and the location/depth of dècollement levels. Opposing thick-skinned, thin-skinned and mixed-thin-thick-skinned tectonic models have been proposed (Fantoni & Franciosi, 2010; Livani et al., 2018; Turrini et al., 2014, among others). Thin-skinned tectonic interpretations point to the key role played by detachments in the sedimentary cover in the thrust-fold systems structuring, but the presented tectonic models differ as regard the number, location and depth of dècollement levels (see Argnani et al., 2016; Livani et al., 2018).

In the following, we briefly describe the main thrust-related folds deforming the sedimentary cover. A review of the published tectonic interpretations is reported in Section 7.3 where we compare our seismic source models to those published in the literature.

Seismic commercial profiles crossing the Mirandola Arc image a 35-km-long and 10-km-wide thrust related anticline (Figures 1b and 1c). The arcuate thrust system rotates from WSW-ENE trending to W-E in the frontal

part, to NW-SE and it is segmented in second-order structures by transverse faults (Nardon et al., 1991). Blind fore- and back-thrusts splay from a deep main thrust and deform the fold forelimb and backlimb, respectively (Figure 1c; Carminati et al., 2010; Nardon et al., 1991; Astiz et al., 2014). These secondary faults also cut Late Pliocene-Pleistocene marine sediments (Bonini et al., 2014).

The Ferrara Thrust System strikes WNW-ESE and is structured into three second-order sub-parallel systems (Figures 1b and 1c): the Inner, Middle and Outer thrust systems here referred to as the San Martino, Pilastri and Sermide structures, respectively (Bonini et al., 2014). Like the Mirandola Arc, the architecture of the San Martino and Pilastri structures is defined by secondary fore- and back-thrusts merging at depths with a main SSW-dipping thrust fault (Figure 1c). The Mirandola, San Martino and Pilastri systems share a very shallow anticline originated by intense contractional deformation and uplift during Middle-Late Pliocene times (Figure 1c). Upper Pleistocene–Late Pleistocene marine and continental deposits folded along the crests of anticlines suggest very recent-to-current deformation (Bonini et al., 2014; Carminati et al., 2010). Conversely, the Sermide outermost thrust-fold is a deeper and less deformed structure (Figure 1c).

North-south active shortening along the Ferrara-Romagna Arc agrees with borehole breakouts (Montone et al., 2004), GPS measurements (Devoti et al., 2011) and geomorphic anomalies (Burrato et al., 2003). The minimum horizontal stress direction inferred by breakouts data tends to be parallel to the thrust fronts and to the axis of the antiforms. GPS data suggests low convergence rates in this region (<2.5 mm/yr), in agreement with the moderate historical and instrumental seismicity in the Ferrara-Romagna Arc (Figure 1a) (Rovida et al., 2011). Only sparse weak events were recorded prior to the 2012 sequence, apart from a moderate M_w5.4 transpressive earthquake that occurred in 1996 under the western termination of the Mirandola Arc (Selvaggi et al., 2001) (Figure 1a).

3. Mainshocks and Aftershocks: Spatial Distribution and Focal Mechanisms

Numerous stations of the national networks run by INGV, and Italian Civil Protection operated in the epicentral area (Figure 2). These networks were complemented by INGV temporary stations installed soon after the May 20th mainshock to improve earthquake monitoring (Moretti et al., 2012). The sequence includes thousands of aftershocks distributed over a W-E elongated region 50-km-long (Figures 3 and 4). Early aftershocks of the May 20th mainshock rapidly migrated to the south of the Ferrara Thrust System toward the Mirandola anticline, where the second mainshock occurred on May 29th. While the hypocentral location of the May 29th event is firmly constrained by the additional temporary local stations, larger uncertainty affects the location of the first mainshock. Of the different locations reported for the May 20th mainshock (Marzorati et al., 2012; Govoni et al., 2014; Lavecchia et al., 2015; among others), we consider that of Styles et al. (2014) as the most accurate because it was determined through a robust probabilistic, non-linear location technique (Lomax et al., 2000) combined with a 3D velocity model. Styles et al. (2014) report the following hypocentral parameters: longitude 11.253°, latitude 44.885°, depth 5.3 km with an uncertainty (1σ) of 1 km (Figure 3, section b). The faulting mechanism of the May 20th mainshock was investigated in detail by Scognamiglio et al. (2016) that computed both Time Domain Moment Tensor (TDMT) and Centroid Moment Tensor solutions using a 3D velocity model. Their focal solutions define a nearly pure WNW-ESE striking inverse mechanism with the preferred plane dipping 44° to the SSW (Figure 3).

The May 29th second mainshock is deeper than the first one. In the catalog of Chiarabba et al. (2014) including tomographic 3D re-locations, the mainshock hypocenter is located at 9.9 km depth underneath the central-eastern part of the Mirandola fold (Figure 4, section g). Aftershocks concentrated westward, under the central part of the arc that was struck by four M5+ events (map in Figure 4). Moment tensor solutions of the May 29th mainshock show nearly pure W-E striking thrust-faulting. By using 1-D local velocity models, Scognamiglio et al. (2012) and Malagnini et al. (2012) estimated dip-angles of 38° and 45° for the S-dipping plane nodal plane, respectively (Figure 4, section g).

The 3D aftershock relocations of Chiarabba et al. (2014) and Carannante et al. (2015) are confined between 4 and 14–15 km depth. The 4 km deep cut-off points to the rupture of blind faults. Both authors recognized two main hypocenter alignments interpreted as the mainshocks thrust planes. According to Chiarabba et al. (2014), the sources of the May 20th and May 29th mainshocks dip ∼30° and ∼50° SSW, respectively, whereas Carannante et al. (2015) propose steeper fault planes dipping about 45° and 70°, respectively.

In Figures 3 and 4 we projected the aftershock locations of the catalog of Chiarabba et al. (2014) on vertical sections striking orthogonal to the thrust fronts. This catalog includes 1,528 well located aftershocks with local magnitude in the 0.9–5.3 range that were recorded between May 20th and June 20th 2012 by 44 permanent and temporary local stations. For all aftershocks, P- and S-phases were accurately revised and re-picked by hand to obtain an improved arrival-time data set with respect to that of the ISIDe-INGV catalog (Govoni et al., 2014). The arrival-time data set was input for a local earthquake tomography featuring a $5 \times 5 \times 3$ km regular node spacing. The final catalog of 3D hypocentral re-locations is very accurate: about 94% of locations have horizontal formal error less than 100 m, while about 85% have vertical error less than 200 m.

To constrain the fault geometric parameters of the finite-fault kinematic inversions, we carefully analyzed the aftershock distribution by projecting only hypocenters very close to each section (within 1.0–2.5 km).

The aftershocks of May 20th mainshock tend to align on a SSW-dipping plane with dip-angles between 35° and 45° in the central sector of the source region (Figure 3, sections b and c). To the east, hypocenters evidence a straight fault plane with a dip-angle of 40°–50° (Figure 3, sections d). The fault structure is illuminated between 4 and 13–14 km depth, its location is coherent with the mainshock hypocenter of Styles et al. (2014) and the surface projection matches the Pilastri thrust system (map and section b in Figure 3). A shallower cluster dips steeply (about 65°) to the SSW at the western edge of the source region (Figure 3, section a). In this zone the rate of aftershocks strongly increased after May 27th (Figure S1 in Supporting Information S1) and the steep alignment of events persisted after the May 29th mainshock (Figure 4, section h). These aftershocks are mostly located in the hanging-wall volume of the Mirandola main thrust (Figure S1 in Supporting Information S1) and may be related to the secondary high-angle fault segments cutting the fold forelimb. Hence, this off-fault seismicity triggered by the May 20th mainshock activated minor fault segments of the Mirandola system well before the second mainshock.

After the May 29th mainshock, seismicity clusters under the Mirandola fold (Figure 4, sections e–h). Aftershocks illuminate a clear straight plane that dips 40°–45° southward between 5 and 11 km depth under to the frontal portion of the Mirandola Arc (sections e and f). The section g across the mainshock hypocenter also shows a general alignment dipping about 40° to SSW. The mainshock nucleated at the base of a zone illuminated by early aftershocks that include several moderate events ($M_L > 4$). Along section *g*, a small alignment dipping steeply NNE between 4 and 6 km depth might indicate a shallow back-thrust.

Moment tensor solutions of numerous M4+ aftershocks (Malagnini et al., 2012; Scognamiglio et al., 2012) evidence the rupture of reverse faults striking mainly E-W and having dip-angles in good agreement with those of the structures inferred from earthquakes alignments described before (Figures 3 and 4).

Nodal planes dipping from 40° to 60° to SSW further support the conclusion that the aftershocks delineate moderately to steeply dipping thrust faults extending downward to 13–14 km depth at least.

4. Mainshocks Recordings and Geodetic Data

4.1. Strong Motion and High-Rate GPS Data

We used strong motion data recorded by permanent stations of the national accelerometric network (https://rischi.protezionecivile.gov.it/en/seismic/activities/emergency-planning-and-damage-scenarios/ran-national-accelerometric-network) and of the INGV Italian seismic network and by local stations installed soon after the first mainshock (Moretti et al., 2012). We selected 8 and 14 strong motion stations for the May 20th and the May 29th mainshocks, respectively (black triangle, in Figures 2a and 2b). Three of the six temporary stations selected for the May 29th event have been used for the first time in this study (green triangles in Figure 2b).

The accelerograms were integrated over time to obtain ground velocity time histories and then bandpass filtered between 0.01 and 0.25 Hz. The choice of the frequency band relies on strong ground motion amplification effects caused by very thick Plio-Pleistocene sediments of the Po Plain basin (Milana et al., 2014).

During the May 20th earthquake, many of the GPS stations collected data at high sampling rates (sampling frequencies from 1 to 20 Hz), recording the dynamic displacements associated with the event (Avallone et al., 2012). In this study we considered high-rate GPS data (white dots in Figure 2a) recorded by four 1 Hz continuous receivers.

4.2. Geodetic Data

We used 16 and 19 three-component GPS static measurements of the coseismic surface displacement, for the May 20th and the 29th event, respectively (purple dots in Figures 2a and 2b, respectively). These horizontal and vertical coseismic displacements represent a sub-set chosen from the GPS measurements published by Serpelloni et al. (2012). We also considered Synthetic Aperture Radar (SAR) data, provided by Italian Space Agency (ASI) and by the Canadian Space Agency, used for rapid generation of coseismic displacement maps, immediately after the quake occurrences (Pezzo et al., 2013; Salvi et al., 2012). In detail, we considered the coseismic deformation associated to the May 20th and the 29th event, observed from Radarsat-1 and COSMO- SkyMed (hereinafter CSK) satellite, both in descending orbit geometry. The Radarsat-1 pair span between 2012 May 14th, and June 5th, timely and spatially covering the entire seismic sequence. The CSK data set consists of two interferometric pairs acquired on 2012 May 19th and May 23rd, and on 2012 May 27th, and June 4th, temporally detecting the first and the second mainshock. The latter (hereinafter CSK2) covers the epicentral area of the second shock, whilst the first (hereinafter CSK1) partially detects the first earthquake displacement field. Thus, the deformation along the satellite Line of Sight (LoS) associated to the first earthquake have been obtained by subtracting the displacement observed from CSK2, during the second event, to the displacement measured by Radarsat-1 (14/05/2012–05/06/2012). The details of the image processing and procedure validation can be found in Pezzo et al. (2013).

In this work, we inverted for re-sampled DInSAR data, by adopting a regular sampling on a 450 m mesh grid obtained from Radarsat-1-*minus*-CSK1 and CSK2 data. The re-sampled data represents the static ground deformation along the LoS of the satellites, on 3,690 and 3,555 points, for the May 20th and 29th events, respectively (see Data Set S1 and S2). We computed the synthetic deformation along the satellite LoS direction.

5. Subsurface Geological Sections and Fault Planes Set-Up

We constructed two geological sections crossing the Mirandola and Ferrara thrusts systems by interpreting the only two seismic reflection profiles freely available in the epicentral region and numerous deep oil wells. Our goal was two-fold: (a) to constrain the geometry of the faults used in the inversions, (b) to pinpoint the thrust faults ruptured by the mainshocks and investigate the role played by lithology and structural discontinuities in the rupture process and aftershock distribution.

Finite-fault inversions of strong motion and geodetic data critically depend on the reliability of source geometric parameters. To address this key point, we defined source geometric parameters that honor both seismological and subsurface geologic data.

We constrained the position and strike of the input sources, defined as blind planar faults, through the two geological sections complemented by published subsurface structural maps. The fault dip defined by the geological sections at first, was chosen to change within a range according to the following seismological constraints: (a) all selected faults are tied to the mainshock hypocenter (i.e., the fault depth in correspondence with the hypocenter must fall within the hypocentral depth range given by the vertical location error), (b) the dip range agrees with that of mainshock moment tensor solutions of Scognamiglio et al. (2012, 2016), (c) the dip range is consistent with that of the mainshock fault plane inferred by aftershock alignments described in Section 3. Obviously, the fault strike also agrees with the mainshock focal mechanism.

With this procedure, we considered the ambiguity in the deep geometry of the thrust faults that also depends on depth-conversion of the interpreted seismic sections through the P-wave velocity associated to geological units, the uncertainty in mainshock hypocentral location, and possible systematic shifts in 3D aftershock locations.

In order to find the best fault plane to be used afterward for the joint inversion, we performed several preliminary inversions by taking into account input sources with different geometries consistently with the aforementioned fault parameters variability. We selected the final seismic source model that provides the best agreement between observed and modeled data.

5.1. The May 20th Mainshock

We interpreted the time-migrated deep seismic section "App Orien-1" available from the ViDEPI Project (2015) (Figure S2 in Supporting Information S1). The seismic profile strikes NNE-SSW nearly orthogonal to the Ferrara

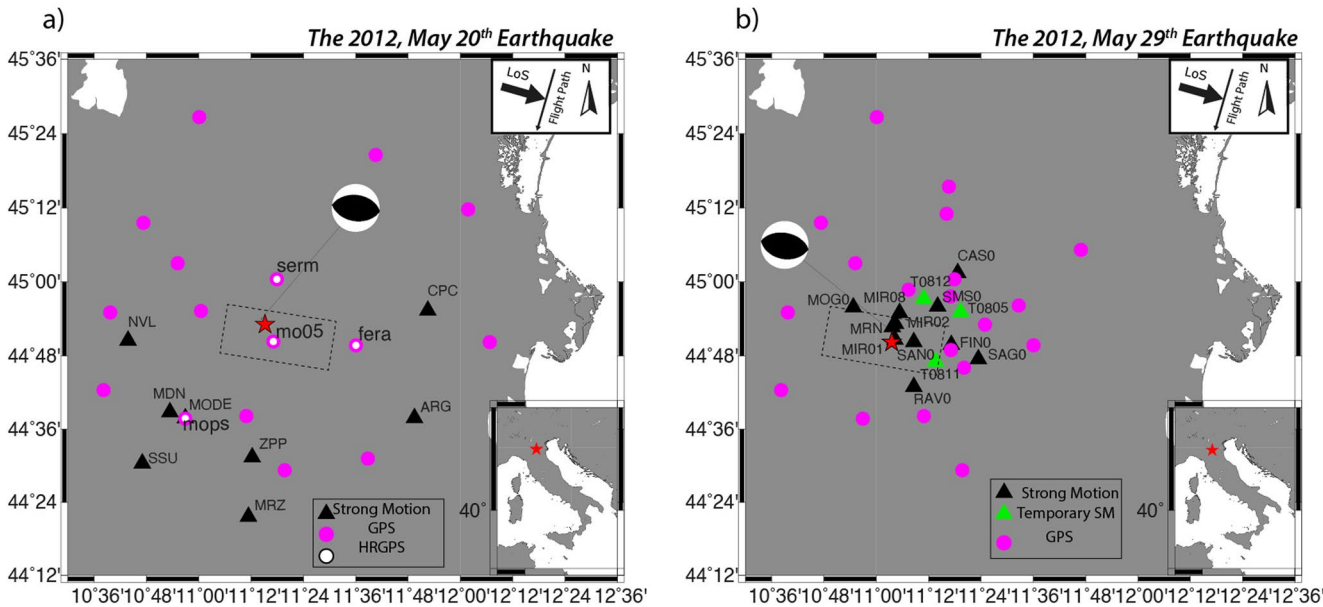

Figure 2. (a) Seismic and GPS stations used to determine the May 20th mainshock rupture model; (b) seismic and GPS stations used to determine the May 29th mainshock source model; green triangles display temporary strong motion stations installed soon after the May 20th mainshock. Inset in the upper right show SAR data range. Red stars correspond to the mainshock epicenters; black dashed boxes are the surface projections of the modeled sources.

Thrust System and oblique to the lateral ramp of the Mirandola Arc and is only 1.8 km apart from the mainshock epicenter (Figure 1b). Noteworthy, we relocated the seismic profile based on the actual shots positions (GeoMol Project; ISPRA, 2015) because in the ViDEPI database it is misplaced about 3.6 km in the NW direction.

Our interpretation is calibrated with eight exploration wells (ViDEPI Project, 2015) (Figures 1b and 5). Further constraints include time- and depth-structural maps of the top of the Jurassic limestones under the Mirandola and the Inner Ferrara thrust systems based on a grid of proprietary seismic reflection lines (Bencini, 2009) and the geometry of the Mirandola and Ferrara thrust systems, as reported in the Structural Model of Italy (Bigi et al., 1991; Figure 1b). We analyzed the sonic logs of 6 deep wells in the area (Styles et al., 2014; ViDEPI Project, 2015) to define the P-wave velocity values of the geologic units for the depth conversion of the interpreted section (Figure 1b, Table S1 in Supporting Information S1).

The seismic section provides high-resolution stratigraphic and structural images of the Meso-Cenozoic sedimentary cover and uppermost basement in correspondence with the Plio-Pleistocene deep synforms (i.e., down to 6–7 s TWT to the SW of the Mirandola system; Figure S2 in Supporting Information S1). Conversely, deep seismic imaging is fair in the footwall volume of the main thrust ramps underneath the Mirandola and Pilastri anticlines. Nevertheless, reflector offsets, abrupt changes in reflection configuration and zones of disrupted reflections allowed us to interpret the thrust ramps in the deeper part of the section (Figure 5a).

From top to bottom we identified the following seismo-stratigraphic units: Quaternary deposits, Middle-Upper Pliocene and Lower Pliocene siliciclastic units, Middle Eocene–Miocene marly and terrigenous successions, shallow- to deep-water carbonates (Jurassic–Lower Eocene), Upper Triassic dolomites, Paleozoic–Middle Triassic basement s.l. (Figure 5a).

The Mirandola fold relates to a deep thrust-ramp rooted down into the basement (Figure 5b). The ramp offsets the Mesozoic carbonates and the basement with relatively straight geometry and an apparent dip in the 35°–45° range. Along the fold forelimb four blind thrusts cut the Mio-Pliocene units with dip-angle ranging from 50° to 80°. These shallow fore-thrusts and a back-thrust splay from the deep ramp at depths between 5 and 6 km, and upthrow the Mesozoic limestones at ~4 km depth in the core of the anticline (well Spada 1; Figure 5b). The intense deformation, uplift and emersion of the Mirandola anticline during the Middle-Late Pliocene is evidenced by the absence of coeval sediments and eroded Lower Pliocene strata that present truncation terminations under the fold crest (Figure 5a). The fore-thrusts offset Late Pliocene–Pleistocene marine deposits, while

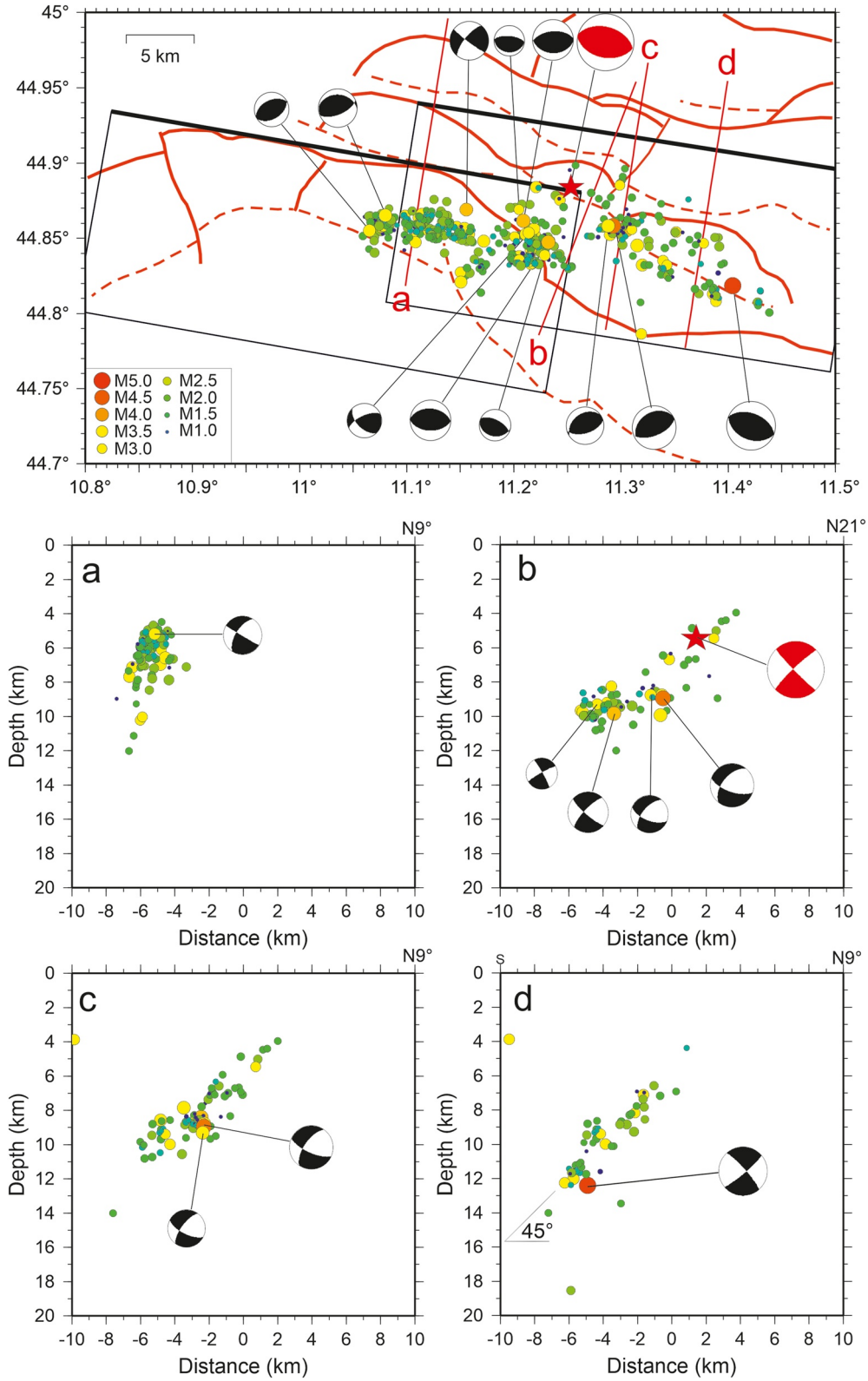

Figure 3. Map view and vertical sections of the aftershocks recorded between the May 20th and May 29th mainshocks. Earthquakes are sized and colored by magnitude. The projected hypocenters are within 2.0–2.5 km distance from the cross sections. Focal solutions are from Scognamiglio et al. (2012, 2016) and Malagnini et al. (2012). The mainshock is depicted by a red star and beach-ball. The main thrust fronts are shown in the map (see labels in Figure 1b). The rectangular frames correspond to the surface projection of the two modeled finite-faults (the black thick line defines the upper tip of the blind source).

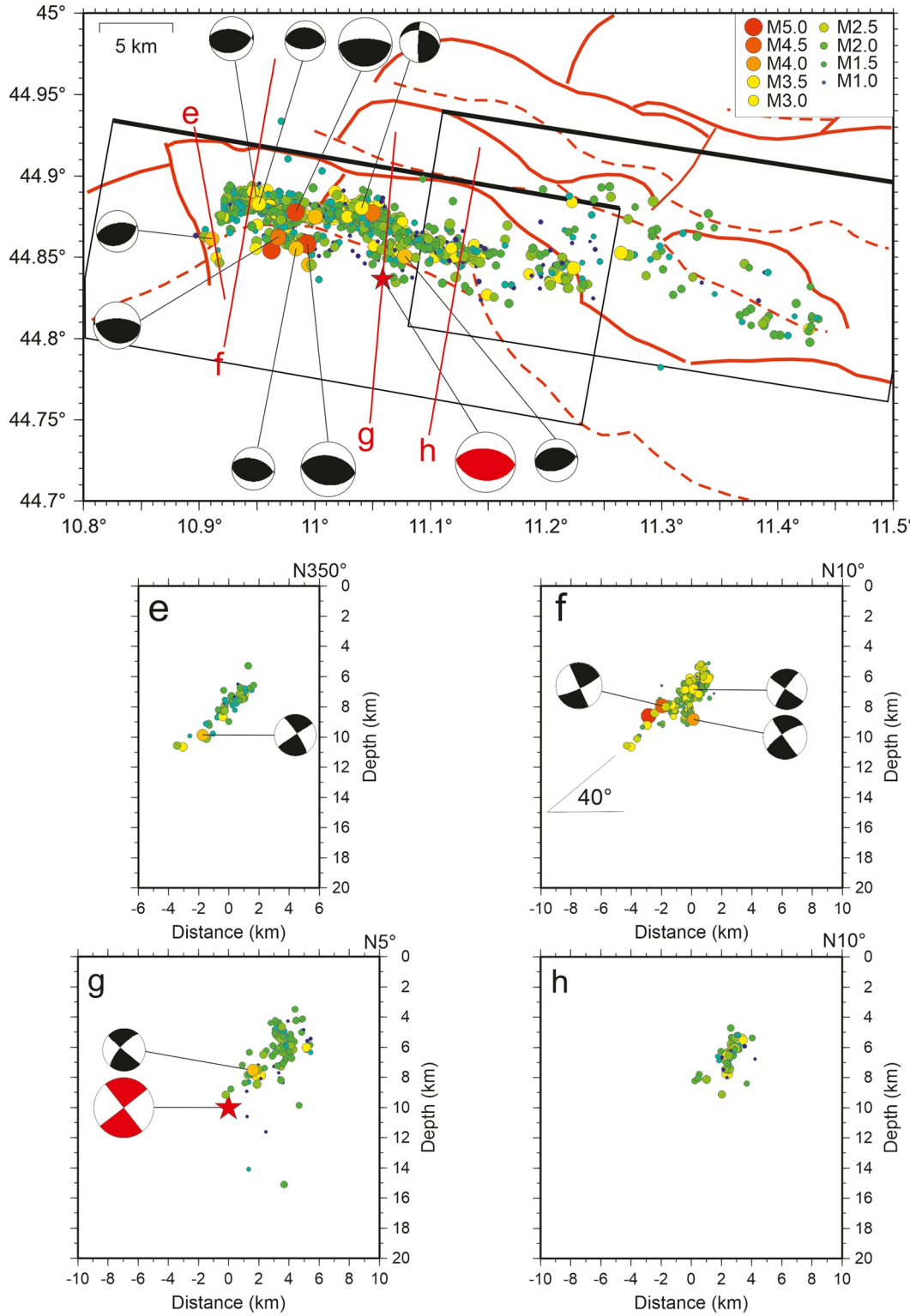

Figure 4. Map view and vertical sections of the aftershocks following the May 29th mainshock and recorded up to 20 June 2012. Earthquakes are sized and colored by magnitude. The projected hypocenters are within 1.0–2.0 km distance from the cross sections. Focal solutions are from Scognamiglio et al. (2012) and Malagnini et al. (2012). The mainshock is depicted by a red star and beach-ball. The main thrust fronts are shown in the map (see the labels in Figure 1b). The rectangular frames correspond to the surface projection of the two modeled finite-faults (the black thick line defines the upper tip of the blind source).

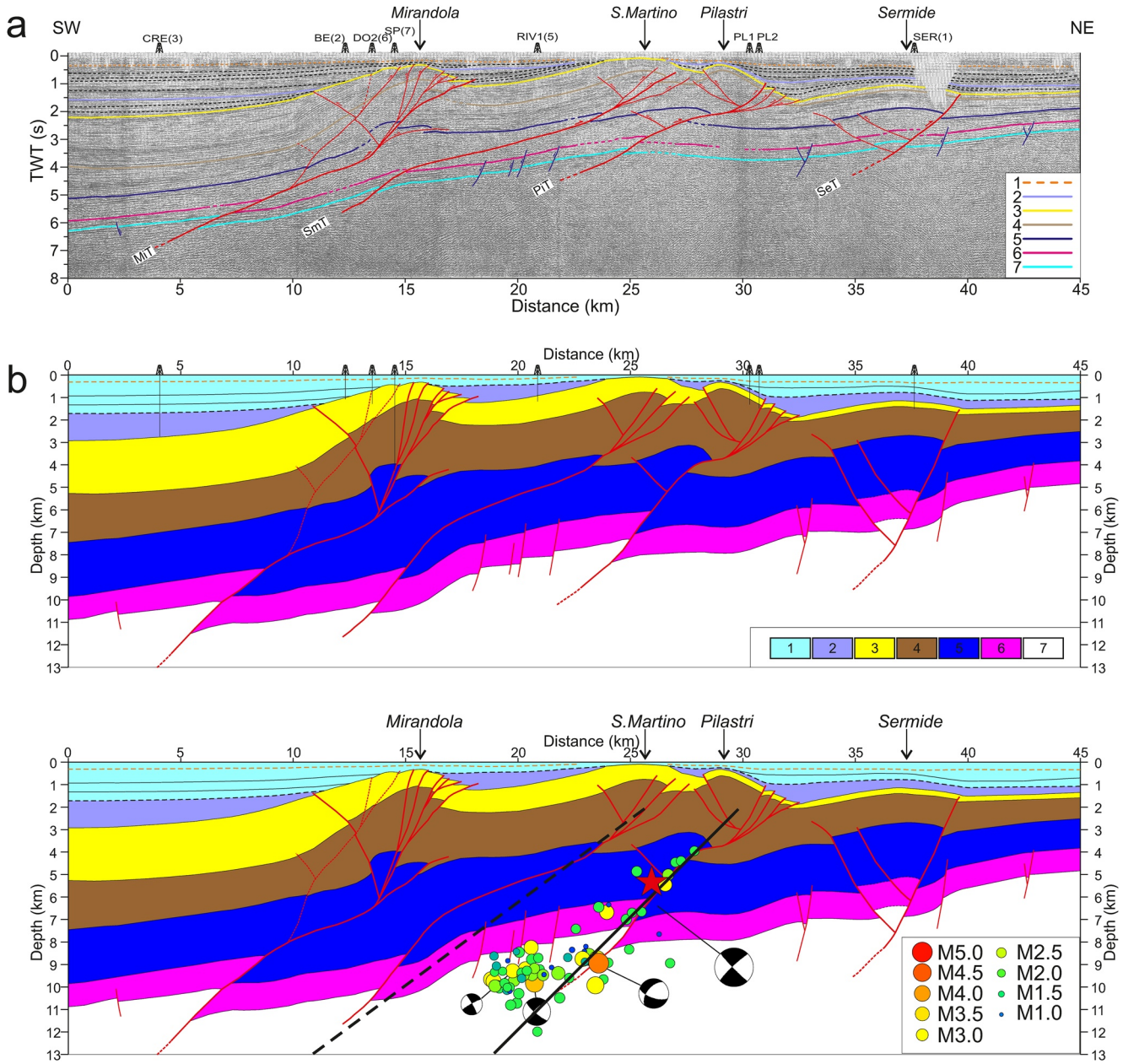

Figure 5. Interpretation of the seismic profile App Orien-1 crossing the Ferrara thrust system and the Mirandola dextral ramp. The profile trace is indicated in Figure 1b (label *c*). (a) Two-way-time seismic section with line-drawing: 1—Upper Pleistocene continental deposits (presumed bottom of), 2—top Middle-Upper Pliocene, 3—top Lower Pliocene, 4—top Miocene, 5—top carbonates (Jurassic—Lower Eocene), 6—top Upper Triassic dolomites, 7—top Permian - Middle Triassic basement s.l.; Red lines denote reverse faults of the Mirandola (MiT), San Martino (SmT), Pilastri (PiT) and Sermide (SeT) thrust systems. Synsedimentary normal faults cutting the Triassic dolomites and the basement are shown in blue. The interpretation is calibrated with the wells: Crevalcore 1 (CRE), Bevilacqua 1 (BE) Dogaro 2 (DO), Spada 1 (SP) Rivara 1 (RIV1), Pilastri 1 (PL1), Pilastri 2 (PL2) and Sermide 1 (SER1) (from ViDEPI Project, 2015). The number in brackets is the borehole distance (in kilometres) from the seismic profile. (b) Depth converted geological model. Legend: 1—Quaternary, 2—Middle-Upper Pliocene, 3—Lower Pliocene, 4—Middle Eocene to Miocene, 5—Lower Jurassic to Lower Eocene carbonates, 6—Upper Triassic dolomites, 7—Paleozoic to Middle Triassic basement s.l. (evaporites, siliciclastic deposits, volcanites and metasediments overlying pre-Hercynian crystalline rocks). We projected on the geological section the May 20th mainshock (red star), the aftershocks (circles, within 2.5 km), the focal mechanisms, the determined best-fit seismic source model (thick black line) and the seismic source from Bonini et al. (2014) (dashed black line).

very recent deformation is testified by warped continental deposits (Late Pleistocene) and syn-tectonic marine strata (Middle-Upper Pleistocene) displaying convergent onlap terminations on the fold limbs (Figure 5a).

The San Martino and Pilastri anticlines feature a similar configuration of the Plio-Pleistocene reflectors documenting intense shortening and very recent deformation (Figures 5a and 5b). The San Martino system is formed by three fore-thrusts and one back-thrust splaying from a deeper main thrust fault. This latter penetrates the sedimentary succession down to the basement with a ramp-flat-ramp geometry and fault angle ranging from bottom to top between 50°, 25°, and 35° (Figure 5b).

About 4 km to the northeast, the Pilastri anticline develops above a thrust-ramp deeply rooted into the basement. The ramp offsets the basement s.l. and the Upper Triassic–Lower Eocene carbonates with a relatively straight geometry (fault angle of 40°–50°). The Jurassic–Lower Eocene limestones are ∼3 km deep in the fold core. The basement s.l. is imaged at 7–8 km depth in the fault hanging-wall. The fault dip abruptly decreases at the transition to the Middle Eocene - Miocene sediments. Shallow fore- and back-thrusts splay from this flatter portion of main thrust and cut with dip-angles of 35°–50° the Miocene-Late Pliocene units along the forelimb and back-limb, respectively (Figure 5b).

The Sermide anticline relates to a steep thrust fault (fault angle 50°–60°) rooted into the basement whose upper termination dies in the Lower Pliocene deposits. Recent shortening is inferred by large wavelength folding in the Upper Pliocene - Pleistocene marine sequences.

The basement is 5–6 km deep in the footwall of the Sermide thrust, and 10–11 km deep under the Mirandola Arc (Figure 5b). Such a southward dip agrees with the regional trend of the foreland monocline under the Ferrara-Romagna Arc (Mariotti & Doglioni, 2000).

Several lines of evidence support a straight correlation between the Pilastri thrust-ramp and the May 20th mainshock source (Figure 5b): (a) the projected hypocenter is only 600 m south and 800 m above the ramp; (b) the fault strike (N95°–105°, Figure 1b) and dip (40°–50°) are coherent with the values determined in the complete moment tensor study of Scognamiglio et al. (2016) (i.e., strike N101° and dip 44° with associated uncertainty 94°–107° and 41°–48°, respectively); (c) the alignment of aftershocks between 4 and 12 km depth and the source mechanisms of M4+ events agree with the ramp geometry (see also sections b–d in Figure 3); (d) off-fault aftershocks in the fault hanging-wall volume are 4–5 km far away from the San Martino main thrust.

The source geometrical parameters adopted in the finite-fault inversions are the following: strike N99°, dip range 35°–45°, depth range of the upper tip 2.0–2.5 km.

5.2. The May 29th Mainshock

We interpreted the freely available profile MO-377-83 published by Nardon et al. (1991). Seismic data in Figure 6 was specifically processed with a Pre-Stack Depth Migration technique effective to cope with the strong lateral velocity variations and steep-dipping reflectors of the Mirandola structure. The N-S trending profile cuts nearly orthogonal the frontal thrust about 6 km to the west of the mainshock location (Figure 1b). We constrained our interpretation through three deep oil wells of the Cavone oilfield (Astiz et al., 2014; Styles et al., 2014), the structural map of the top of the Mesozoic carbonate reservoir (Nardon et al., 1991), the geometry of the Mirandola frontal thrust published by Astiz et al. (2014) that interpreted a grid of proprietary seismic profiles.

The seismic section reaches a depth of 5 km. To extend the geological section down to seismogenic depths we considered the depth-maps of the top basement s.l. and Jurassic limestones of the GeoMol regional model (ISPRA, 2015).

In addition to the geological horizons interpreted in section “App Orien-1,” well and seismic data allowed us to recognize the top of Cretaceous–Lower Eocene limestones (Figure 6).

The architecture of the thrust-fold system is comparable to that imaged across its western ramp (Figures 5 and 6). Two main differences regard the involvement of the Upper Triassic dolomites in the core of the anticline, as documented by the Cavone 1 well (Styles et al., 2014), and the remarkable erosion of the Lower Pliocene and Miocene units. Both observations indicate a more intense shortening along the central sector of the arc. The fold forelimb is deformed by two steep-dipping thrusts (fault dip of 50° and 65°) with upper terminations in the shallow Late Pliocene-Pleistocene marine deposits and by the deeper frontal thrust. These fault segments splay from the Mirandola thrust-ramp that we extrapolated downward as a nearly planar fault present-

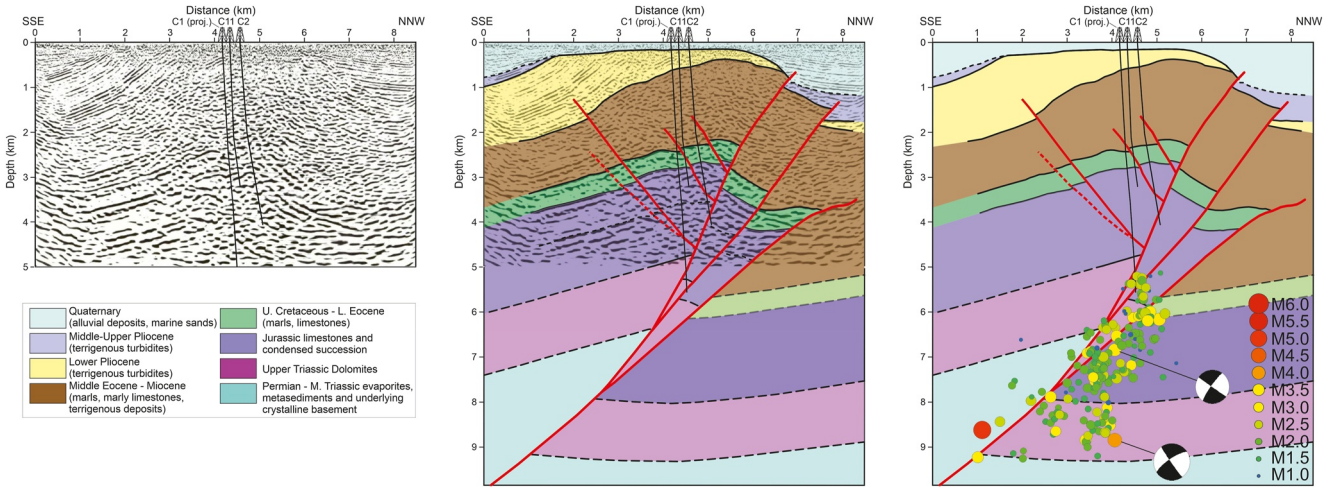

Figure 6. Pre-Stack Depth Migrated section MO-377-83 across the Mirandola Arc. (left) Seismic data. (central plot) Seismic interpretation; the dashed lines represent geological horizons extrapolated at seismogenic depths based on literature data (Astiz et al., 2014; ISPRA, 2015). (right) Geological model with projected aftershocks (circles) and focal mechanisms (within 2.0 km from the section). The interpretation is calibrated with the deep wells Cavone 1 (C1), Cavone 11 (C11), and Cavone 2 (C2) (Astiz et al., 2014; Styles et al., 2014).

ing a dip-angle of about 45° and deeply rooted into the basement (Figure 6). Such a fault geometry agrees with the clear fault plane illuminated by aftershocks (Figure 4, sections e and f) and with the subsurface models of Astiz et al. (2014) and Juanes et al. (2016). Based on a grid of proprietary seismic profiles of excellent quality, these authors defined the Mirandola main thrust as an almost straight ramp down to 17–18 km depth with an average dip-angle of 40°–50° (see the depth-migrated seismic section crossing the western portion of the Mirandola arc shown in the Figure S3 of Juanes et al., 2016). The source geometrical parameters we adopted in the finite-fault inversions are the following: strike N100°, dip range 39°–46°, depth range of the upper tip 2.5–4.0 km.

6. Kinematic Source Inversion

We obtained the rupture history of the May 20th and 29th mainshocks by jointly inverting strong motions, HRGPS, GPS displacements and DInSAR data. We adopted a nonlinear technique (Cirella et al., 2012; Piatanesi et al., 2007) whose details are reported in the Supporting Information S1 (Text S1).

6.1. Inversion Parameters

We performed two distinct joint inversions of strong motion and geodetic data to retrieve the rupture history of the May 20th and 29th mainshocks by considering different ranges of variability for each kinematic parameter. We simultaneously inverted for the rupture time, peak amplitude and direction of slip velocity and rise time, on a grid of points regularly spaced (3.0 and 2.5 km for the May 20th and the May 29th earthquakes, respectively) along strike and downdip directions. The distribution of the final slip was derived from the inverted model parameters (rise time and peak slip velocity) according to the assumed source time function. In this work we adopt a regularized Yoffe function (Tinti et al., 2005) having a constant time to peak slip velocity (T_{acc}) equal to 0.225 s.

For the May 20th event, bounds of 0–1.5 m/s are allowed for peak slip velocity; the rise time varies between 0.75 and 3 s and rake angles from 72° to 112°. The rupture velocity is between 1.5 and 3.5 km/s.

To image the May 29th earthquake rupture process, peak slip velocity ranges between 0 and 1.5 m/s; the rise time between 0.8 and 3.8 s and the rake angle from 70° to 110°.

The propagation time from the hypocenter of a rupture front having a speed between 1.5 and 3.5 km/s is used to bound the rupture onset at each grid node. We assumed the hypocenters of Styles et al. (2014) and Chiarabba et al. (2014) as nucleation points of the May 20th and 29th mainshocks, respectively.

Slip direction variability has been chosen by assuming a faulting mechanism consistent with focal solutions determined by waveforms inversion (Scognamiglio et al., 2012, 2016).

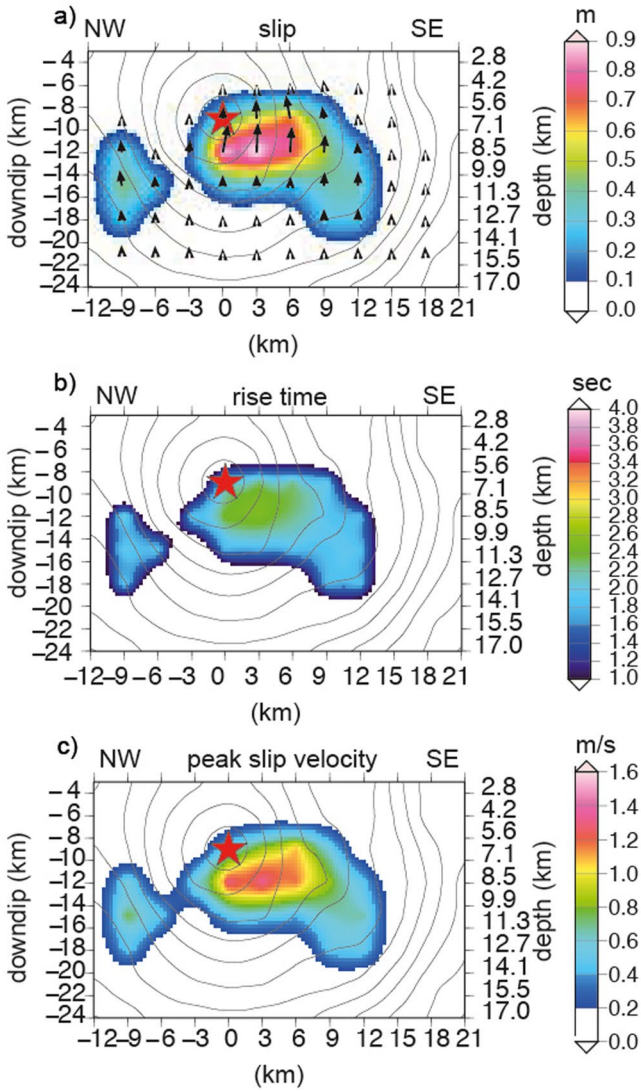

Figure 7. May 20th earthquake source model given in terms of estimated slip, rise time and peak slip velocity distributions on the fault plane (panels a–c, respectively). Black contour lines in the top panel show the retrieved rupture time every 1 s; rake is indicated by black arrows in panel (a).

The very heterogeneous geological and velocity structure of the Po Plain basin causes complex seismic wave propagation effects evidenced by strong variations in the low-frequency (<0.5 Hz) seismic response (Milana et al., 2014). In such a setting, the use of well-calibrated GFs in the inversion is of key importance to adequately separate source and propagation effects (Gallovič et al., 2015). To tackle this difficulty, we calculated site-specific GFs through 1-D crustal profiles of P-, S-wave velocity and density defined below each seismic station. We constructed an ensemble of vertical profiles upon the 3-D regional geophysical model of the Po Plain and surrounding regions developed by Molinari et al. (2015) (details on the model building are reported in the Text S2 in Supporting Information S1). The obtained velocity profiles vary significantly in the topmost 6 km of the crust depending on the thickness of the low-velocity Plio-Pleistocene terrigenous sediments (Figure S3 in Supporting Information S1).

In order to check the quality of the azimuthal data coverage we performed checkerboard resolution tests for both events; the obtained results are shown in Supporting Information S1 (Text S3).

6.2. Rupture Process of the May 20th M_w6.1 Mainshock

The algorithm explored about 1.5 million rupture models to form the model ensemble. Figure 7 shows the inverted rise time and peak slip velocity distributions and the calculated slip distribution, for the best-fit planar fault that has a dip-angle of 45°. The retrieved source model (averaged from ensemble inference, see Text S1 in Supporting Information S1) presents two patches of slip: a small deeper patch located 5–11 km west from the nucleation and a larger one that develops downwards and to the southeast of the nucleation point (Figure 7, top panel). The larger and smaller asperities are characterized by a maximum slip of 0.87 and 0.65 m, respectively. The resulting seismic moment (1.9×10^{18} Nm) yields a moment magnitude (M_w = 6.1) in fair agreement with those inferred in previous works (Cesca et al. (2013); Cheloni et al. (2016); Pondrelli et al. (2012); Saraò and Peruzza (2012), see Table S2 in Supporting Information S1). The slip direction (black arrows in the upper panel of Figure 7) is consistent with a thrust mechanism.

The rupture duration is about 9 s (black contours in Figure 7). In coincidence with the larger asperity, located in the south-eastern portion of the fault, the rupture front accelerates from 1.7 to 3 km/s (see Figure S9 in Supporting Information S1). This rupture acceleration may explain the rupture directivity observed by Cesca et al. (2013). The two slip patches are robust features of the obtained model, as supported by synthetic (checkerboard-like) resolution tests (Figure S4 in Supporting Information S1), and by the separate inversions (Figure S8a in Supporting Information S1).

The comparison of each data set is shown in Figure 8. The simulated ground velocities match fairly well the recorded one at most of the stations (Figure 8a). Discrepancies at few sites can be due to the complex 3D wave propagation, as well as to the large-amplitude surface waves generated in the Po Plain shallow sedimentary layers. Furthermore, synthetic and observed coseismic horizontal displacement vectors at the selected GPS stations shows a good agreement (Figure 8b).

Some discrepancies are observed at site CONC, where the coseismic displacement is less constrained, due to the data gap before May 20th (Serpelloni et al., 2012). The modeled DInSAR data (Figure 8d) is comparable with the observed one (Figure 8c) yielding very low residuals especially in correspondence with the fault region where the maximum slip is cumulated (Figure 8e).

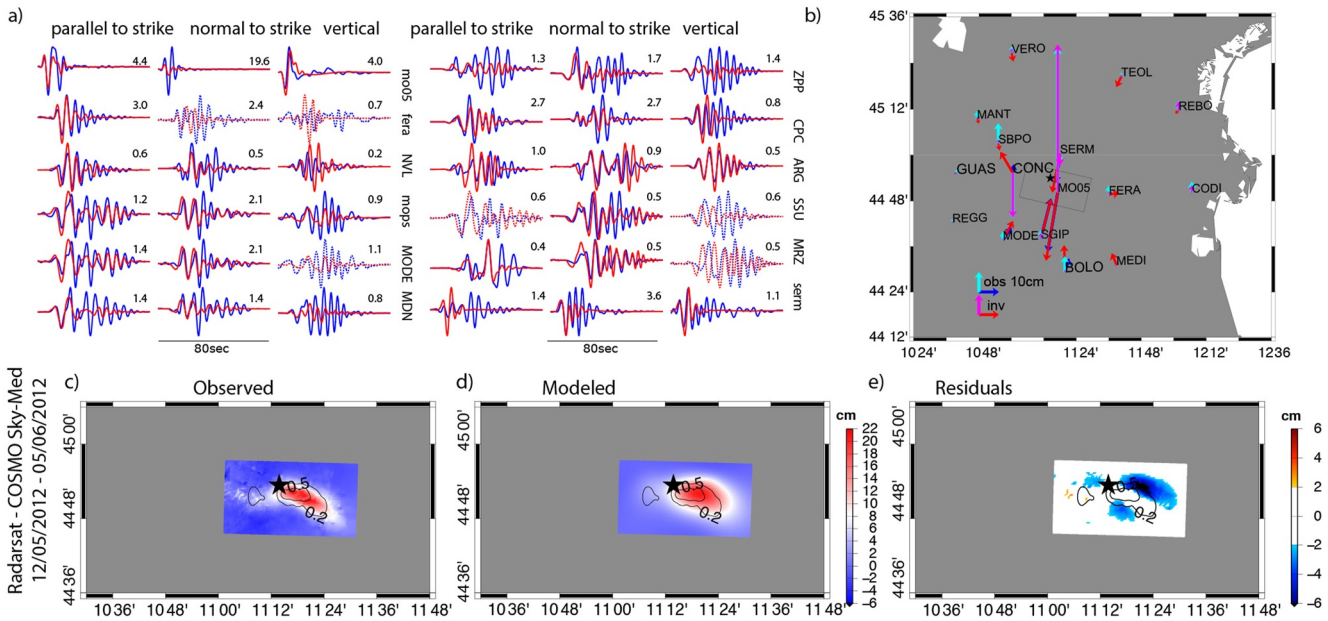

Figure 8. May 20th earthquake data misfit. (a) Comparison of recorded strong motion and HRGPS velocity time histories (blue lines) with synthetic waveforms (red lines). Dashed lines show predicted time series not included during the inversion. Peak amplitudes (cm × s^{-1}) of the observed waveforms are given by numbers; (b) measured and synthetic horizontal (blue and red arrows, respectively) and vertical (cyan and pink arrows, respectively) co-seismic static displacements; (c–e) observed, synthetic and residual DInSAR displacement.

6.3. Rupture Process of the May 29th M_w6.0 Mainshock

The inferred average (1.0 million rupture models have been tested by the search algorithm) rupture model is shown in Figure 9. The three panels (top, central and bottom) show the computed slip, and the retrieved rise time and peak slip velocity distributions for the best-fit source model (fault dip ∼42°). The source model is characterized by two distinct patches of slip: a round-shaped patch in the deeper western part of the fault plane and a shallower patch in the central-eastern part and elongated in the south-eastern direction on the opposite side of the nucleation point. This second dip-elongated patch has slip mostly concentrated in the upper part of the fault, just above the nucleation point. The south-eastern patch extends from 4 to 5 to about 15 km depth and has an along-dip length of about 15 km; the second patch is located between 7 and 8 and 15 km depth, about 8 km westward from the hypocenter. This deeper slip area is not an artifact from inversion, but a robust feature of the rupture model as testified by the checkerboard-like tests (see Text S3 and Figure S5 in Supporting Information S1) and by the separate strong motion inversion, which clearly shows how this second deeper slip area is part of the coseismic phase of the May 29th event (see Figures S6 and S8b in Supporting Information S1).

Both asperities are characterized by a maximum slip of ∼0.8 m. The resulting seismic moment (1.4×10^{18} Nm) yields a moment magnitude M_w = 6.0, and fairly agrees with those inferred by Cheloni et al. (2016) and by Causse et al. (2017) (see Table S2 in Supporting Information S1). The slip direction is consistent with a thrust mechanism. The total rupture duration is about 8 s. The comparison of the recorded and synthetic waveforms (Figure 10a) shows a satisfactory agreement, though in some stations the high frequencies are not well reproduced. Furthermore, the synthetic horizontal and vertical displacements match very well with GPS vectors both in amplitude and direction (Figure 10b). The distribution of the residual between the observed (Figure 10c) and the synthetic DInSAR data (Figure 10d) shows a very good agreement (Figure 10e).

7. Discussion

In this study, we inverted for the first time strong motion, HRGPS, GPS and DInSAR data to recover the rupture history of the May 20th M_w6.1 and May 29th M_w6.0 earthquakes of the 2012, northern Italy, seismic sequence. Despite the moderate events' magnitude, the obtained source models reveal complex rupture processes that were captured only in part by previous studies. The comparison of the slip distribution with geological sections and

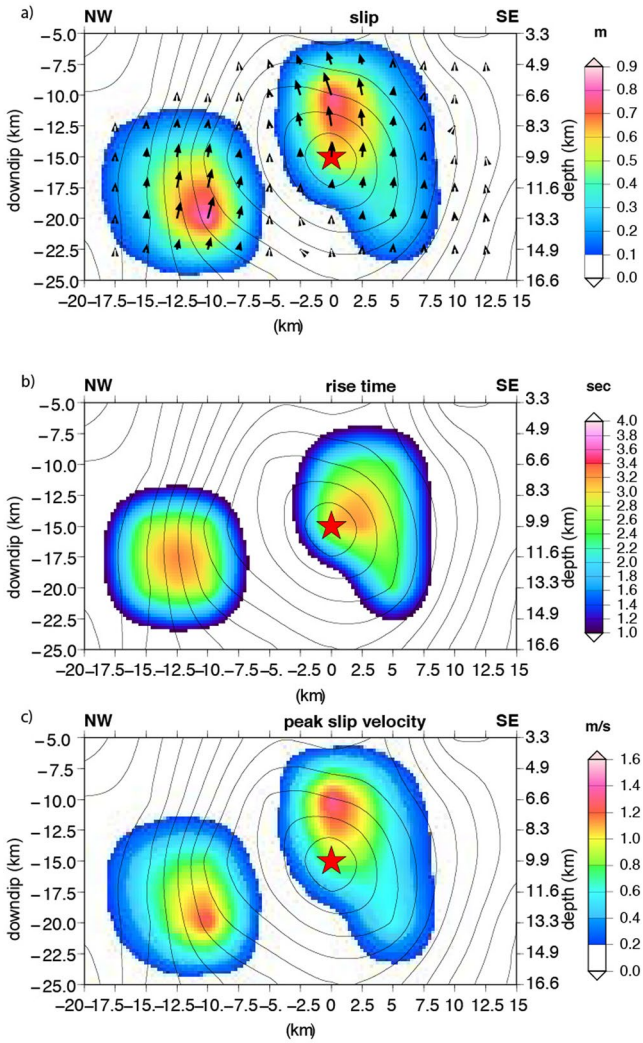

Figure 9. May 29th earthquake source model given in terms of slip, rise time and peak slip velocity distributions estimated on the fault plane (panels a–c, respectively). Black contour lines and arrows in panel (a) display the retrieved rupture time every 1 s and the slip angle, respectively.

aftershock patterns unravels the primary role played by lithological changes and structural discontinuities in controlling the rupture process of both mainshocks and provides key information for a better understanding of the seismic sequence and of the seismotectonic setting of the northern Apennines outer thrust systems.

7.1. Comparison With Previous Seismic Source Models

The source model of the May 20th event agrees in part with the slip distribution obtained in previous works (Figure S7a in Supporting Information S1). Geodetic source models present only one and shallower slip patch (Cheloni et al., 2016; Nespoli et al., 2017; Pezzo et al., 2013, 2018). Rupture heterogeneities were also imaged by Ganas et al. (2012), who inferred the slip distribution by adopting empirical Green's functions (EGFs) and a least squares inversion approach of source time functions (STFs) computed from regional broadband seismological data. Their model features a wide slip area that, similarly to our main patch, extends downwards and to the east of the nucleation point up to 11 km depth, but, differently from our model, no slip is retrieved westward.

We stress that the presence of two separated asperities is coherent with previous findings of Piccinini et al. (2012). Through the analysis of the moment rate functions at two seismic arrays in the Umbria Apennines and Tuscany (central Italy), these authors identified two close, well-correlated pulses occurring in the first 5 s after the P-wave onset.

This source complexity was recently discussed by Convertito et al. (2021), who investigated the slip distribution from the analysis of the STFs obtained by EGFs twofold modeling approach: their results show a source model featuring two slip patches much shallower than ours (black contour lines in Figure S7a in Supporting Information S1). This discrepancy may be due to the different type of data we invert for, to the different geometric fault plane parameterization and not least, to the effects of the adopted frequency range. Furthermore, the approach of Convertito et al. (2021), by using the filtered STFs obtained by the EGFs technique, does not include uncertainties in the structural model as well as the complexity of the observed STFs and the large areas not covered by the seismic stations, could partially influence their results. All these factors strongly affect a kinematic source inversion, in particular the trade-off between the rupture velocity and the position of the retrieved slip patches.

Our rupture time distribution shows acceleration to the south-eastern portion of the fault plane, in agreement with the rupture directivity analyzed by Cesca et al. (2013).

Unlike our results, geodetic source models for the May 29th earthquake feature only one eastern patch and slip at relatively shallow depths (Nespoli et al., 2017; Pezzo et al., 2013, 2018). Figure S7b in Supporting Information S1 displays the comparison with the slip distributions obtained by Pezzo et al. (2018) and Cheloni et al. (2016), both derived by GPS and DInSAR data. In both models, the slipped portion of the fault is thinner and confined between 3 and 8 km (Pezzo et al., 2018) or 7 and 12 km depth (Cheloni et al., 2016). We reckon that the absence of the second patch we find in the western, deeper portion of the Mirandola fault is likely due to the limited resolution capability of geodetic data at depth, as suggested by the checkerboard tests (see Text S3 in Supporting Information S1). Indeed, this deeper slip area is a robust feature of the source model, as documented by synthetic tests indicating enough resolution at that location, especially when we jointly invert all the available data set (Figure S5d in Supporting Information S1).

Regarding the rupture model of Causse et al. (2017), only a first order comparison with our slip distribution is meaningful because of significant differences in the strong motion data modeling and inversion procedure. Their

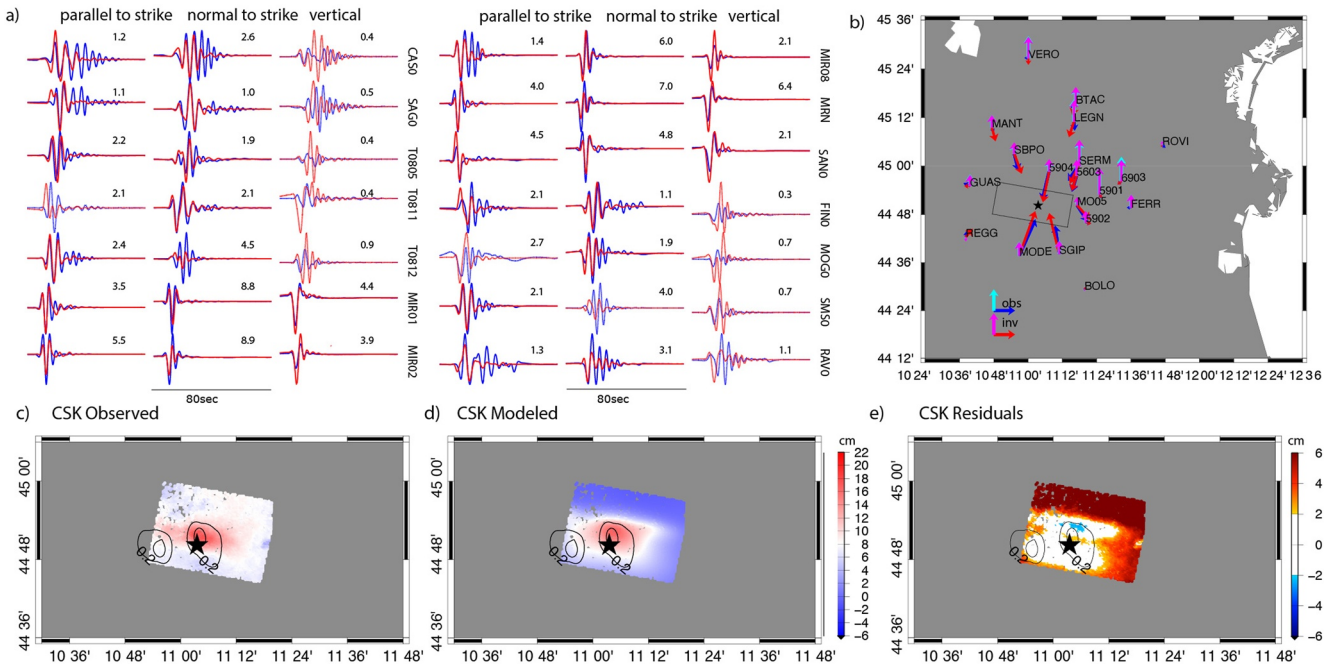

Figure 10. May 29th earthquake data misfit. (a) Observed (blue lines) and inverted (blue lines) strong motion velocity time histories. Dashed lines show predicted time series not included during the inversion. Peak amplitudes (cm × s^{-1}) of the observed waveforms are given by numbers; (b) measured and synthetic horizontal (blue and red arrows, respectively) and vertical (cyan and pink arrows, respectively) co-seismic static displacements; (c–e) observed, synthetic and residual DInSAR displacement.

model shows a single and shallower patch located upwards and to the east of the mainshock hypocenter, with slip confined between 4 and 8 km depth (black contour lines in Figure S7b in Supporting Information S1). These discrepancies in slip distribution may be also due to the different azimuthal coverage and number of stations. The existence of two separated patches breaking co-seismically is corroborated by the inversion of strong motion data (Figure S6 in Supporting Information S1). This agrees also with array analysis and STFs computed using stations within 300 km distance from the mainshock, which concordantly show two distinct pulses separated by a time lag of 2 s (D. Piccinini, personal communication).

7.2. Lithological and Structural Controls on the Rupture Evolution

To investigate the relationship between thrust faults, rock lithology and rupture evolution, we compared the source models to geological sections and aftershock distribution. Regarding the May 20th mainshock, we were able to compare the slip distribution directly to the interpreted seismic section "App Orien-1" because it crosses the main slip patch (section A-A' in Figure 11d). This section was also compared to an along-dip slip profile centered on the smaller western patch (section B-B' in Figure 11d).

The main slip patch has an upper and lower cut-off at depths of 4.5–5.0 km and 13–15 km below sea level, respectively (Figure 11e). The first depth interval corresponds to the transition between the Jurassic - Lower Eocene limestones and the Middle Eocene–Miocene marly and terrigenous sediments, the second is within the basement. The May 20th mainshock ruptured the Pilastri thrust-ramp nucleating from a shallow point in the Jurassic limestones (Figure 11c). The zone of maximum slip is 7–11 km deep (b.s.l.), corresponding to the uppermost basement and the highly competent Upper Triassic dolomites (Figure 11e). The rupture propagated mainly to the east across the carbonate multilayer and downwards, far below the basement top (Figures 11d and 11e). The smaller patch between 7 and 8 and 15 km depth is located in the basement and the Upper Triassic dolomites (Figure 11f).

Aftershocks and slip distribution share the upper cut-off depth of 4 km that represents a first-order rheological boundary separating the Jurassic–Lower Eocene limestones from the Middle Eocene–Miocene terrigenous sediments (Figures 11d and 11e). The former are high-velocity (V_p = 5–6 km/s), high-strength rocks characterized by unstable sliding, the latter low-velocity (V_p = 3.5–4.0 km/s), low-strength sediments defined by a stable sliding mechanical behavior (Table S1 in Supporting Information S1). Such a mechanical behavior is consistent with the

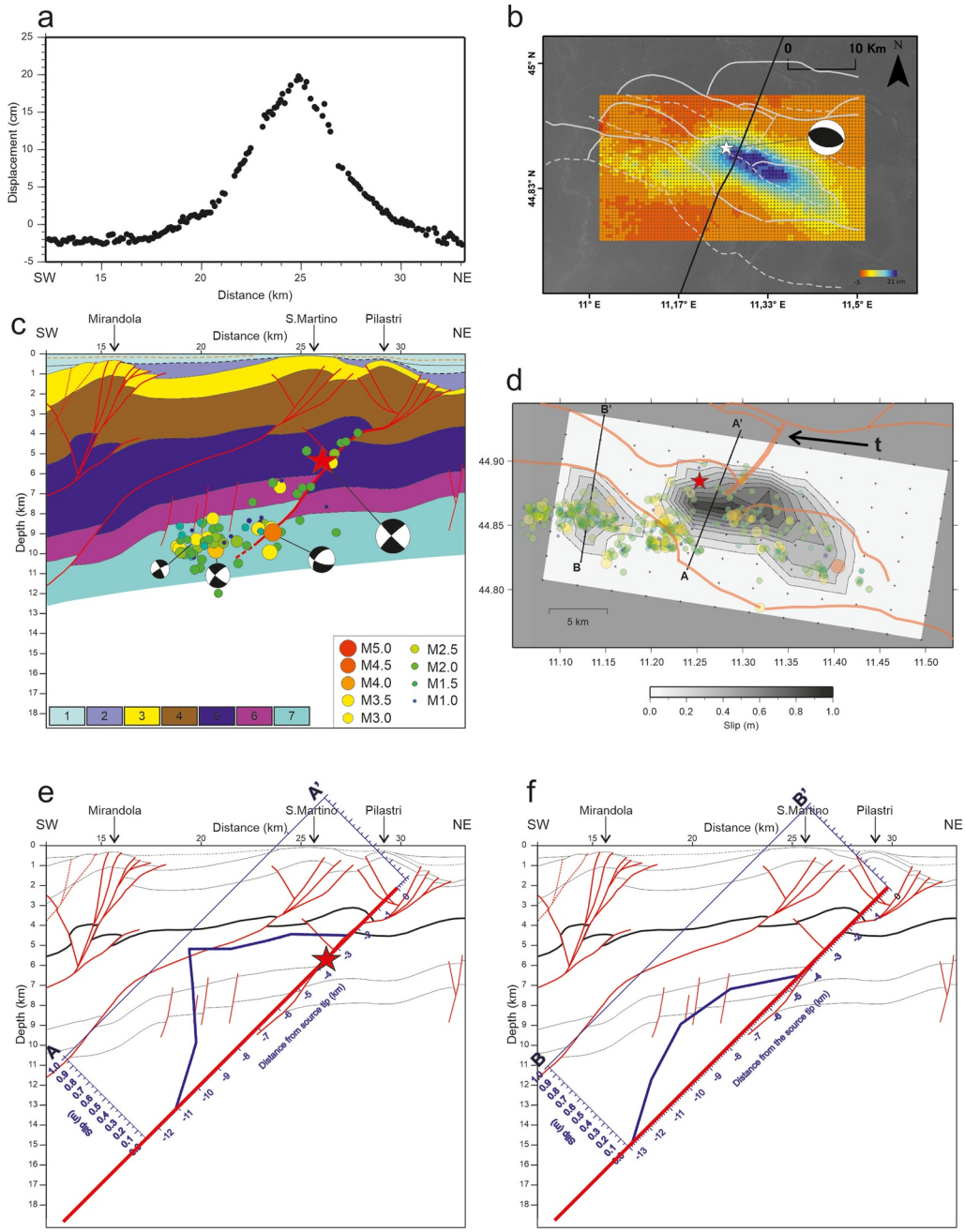

Figure 11. Comparison of the May 20th event slip model with the "App Orien-1" geological section. (a) Coseismic displacement profile for the May 20th event along the seismic section "App Orien-1" obtained from data shown in the following panel (b). (b) Map of the displacement associated with the May 20th event obtained by Radarsat-1 and CSK1 coseismic interferograms (Pezzo et al., 2013). The trace of the seismic profile (black line), the mainshock epicenter (white star), and main buried thrust fronts (gray lines) are plotted on the displacement map. (c) Geological section "App Orien-1" with zoom on the Pilastri fault system (see Figure 5); (d) Map of the slip distribution with the traces of the two slip profiles shown in plots (e and f). The red star is the mainshock epicenter; aftershocks (circles) and main buried thrust fronts (thick lines) are shown in transparency. Label *t* evidences the transverse fault cutting the Pilastri system. (e) The slip profile along the vertical section A-A' that crosses the main slip patch and matches the seismic profile "App Orien-1" is plotted onto the geological model; the thick red line corresponds to the best-fit fault used in the inversion. The red star is the mainshock nucleation point of the kinematic inversion. (f) The slip profile B-B' crossing the western minor asperity is projected on the geological section "App Orien-1" for comparison.

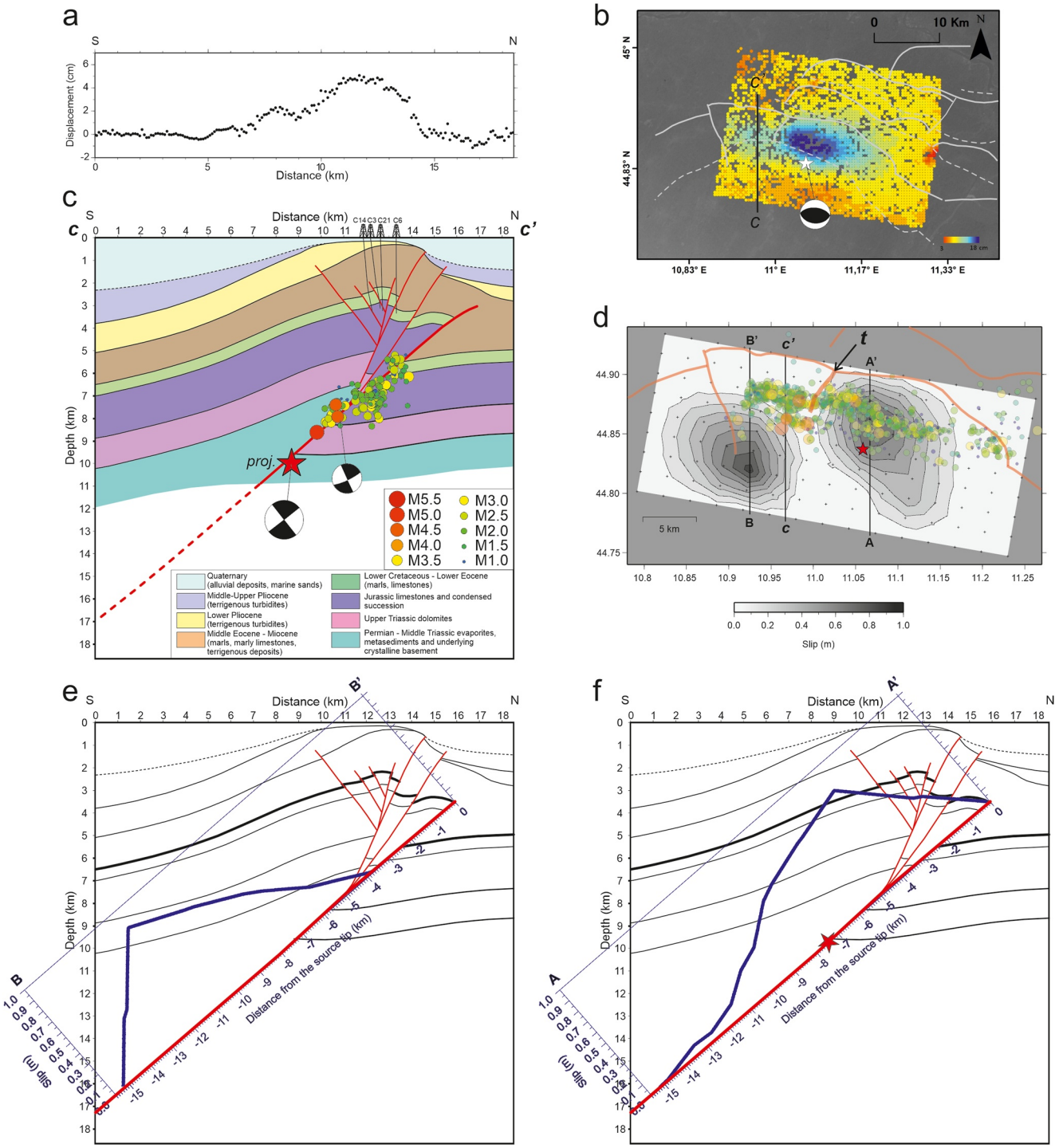

Figure 12. The May 29th event slip model is compared to a N-S geological section crossing the Mirandola Arc. (a) Coseismic displacement profile for the May 29th event along the geological section C-C'. (b) Map of the displacement associated with the May 29th event obtained by CSK2 interferogram (Pezzo et al., 2013). The traces of the geological section C-C' (thick black line), the mainshock epicenter (white star), and main buried thrust fronts (gray lines) are plotted on the displacement map. (c) Geological section C-C' with projected aftershocks (within 1.0 km), mainshock (red star) and focal mechanisms. The geological section is constrained by the nearby seismic profile MO-377-83 (see Figure 6) and calibrated with deep wells C14, C3, C21, C6 of the Cavone oilfield (see Astiz et al., 2014). (d) Slip model with traces of the geological section C-C' and of the two slip profiles shown in panels (e and f). The red star is the mainshock epicenter; aftershocks (circles) and main buried thrust fronts (thick lines) are shown in transparency. Label *t* evidences the transverse fault cutting the Mesozoic carbonates. (e) The slip profile B-B' crossing the western slip patch is projected on the geological sections; the thick red line corresponds to the best-fit fault model used in this study. (f) The slip profile A-A' crossing the eastern slip patch close to the mainshock hypocenter is projected on the geological section. The red star denotes the nucleation point.

presence of a main patch of afterslip observed by Cheloni et al. (2016) at shallow depth (from 1 to 5 km) within the Pilastri anticline.

We speculate that the presence of two separated patches of slip may reflect the along-strike segmentation of the Middle Ferrara thrust system. A fault striking NNE-SSW and dipping steeply westward cuts the Pilastri thrust faults close to the mainshock epicenter (Figure 1b). This transverse structure might represent a structural barrier hampering the rupture propagation to the west of the main patch (Figure 11d). Besides, the complex slip distribution may also be strongly influenced by the recent past history of coseismic slip on the thrust fault and on the nearby active thrust systems.

Aftershocks tend to devoid the high-slip zone (Figure 11d). A cluster of aftershocks fills the gap between the two slip patches at depths of 9–11 km, and the main asperity is bounded to the east by numerous aftershocks that delineate the straight fault plane down to 13 km depth (Figures 11d and 3 section d). Conversely, the westernmost aftershocks represent off-fault seismicity related to steep and shallow fore-thrusts cutting the Mirandola fold (see Section 3 and Figure S1 in Supporting Information S1).

We compared the coseismic dislocation with geological structures in Figures 11a and 11b. The coseismic displacement map shows the main coseismic lobe, southeastward elongated with respect to the mainshock epicenter, that spreads across the San Martino and Pilastri thrust systems. Then, using the geological section, we are able to directly correlate the coseismic displacements with subsurface structures. The maximum displacement is located in correspondence with the San Martino anticline (Figures 11a–11c), in apparent conflict with the activation of the Pilastri main ramp. Such a distribution of displacement agrees indeed with a deep slip, peaked at 8–9 km depth, along a moderately dipping (45°) blind thrust (Figure 11e). The observed displacement reconciles with the strong deformation of Pleistocene strata at the top of the San Martino anticline but cannot justify the surficial deformation of the Pilastri fold. We suggest that while coseismic slip clearly uplifts the San Martino structure, aseismic creep occurs along the shallow fault segments of the Pilastri system, as shown by the afterslip distribution obtained by Cheloni et al. (2016), thus explaining this apparent inconsistency.

We compared the May 29th slip distribution to a N-S trending geological section that is orthogonal to the Mirandola frontal thrust (section C-C' in Figures 12c and 12d). This section is based on the nearby seismic profile MO-377-83 (Figures 1b and 6) and tied to wells of the Cavone oilfield (Astiz et al., 2014). To extend the section on both sides, we used subsurface constraints from regional crustal models (Bigi et al., 1991; ISPRA, 2015). We considered two profiles crossing the western and eastern patches (B-B' and A-A' in Figure 12d, respectively) and projected their slip values onto the geological section according to the strike of the Mirandola frontal thrust (Figures 12e and 12f, respectively).

The eastern patch has an upper cut-off depth of 3.5–4.0 km and elongates down dip up to 15–16 km depth (Figure 12f). The slip concentrates above 11–12 km depth with an evident peak at ∼7 km depth. Remarkably, the upper cut-off matches the top of the Jurassic–Lower Eocene limestones in the thrust hanging-wall volume. The rupture started at ∼10 km depth and propagated mostly to the east and upwards within the Upper Triassic - Lower Eocene carbonates, and downward into the basement (Figures 12d and 12f). The maximum slip occurs where the Mirandola ramp juxtaposes the basement units and highly competent Upper Triassic dolomites above the Jurassic limestones.

The western deeper patch 7–8 to 16 km deep shows a slip peak at 12–14 km; the rupture propagated westward mainly within the basement (Figures 12d and 12e).

The aftershock activity clustered in the upper-western portion of the Mirandola ramp that corresponds to a zone of evident slip deficit in our model (Figure 12d). Several moderate early aftershocks (M_L4–5) occurred in this zone. These events, together with weaker on-fault aftershocks, activated the upper portion of the Mirandola thrust-ramp cutting through the Upper Triassic–Lower Eocene carbonates (Figure 12c). This aftershock zone starts at the upper termination of the western slip patch (Figure 12d) and extends upwards across the Upper Triassic–Jurassic carbonate sequences. Noteworthy, this zone of high aftershock rate is consistent with the region of maximum Coulomb stress increase caused by the combined effect of the two mainshocks, as observed by Cheloni et al. (2016).

Similarly to the May 20th event, we relate the cut-off of slip and aftershocks at 4–5 km depth to the strong lithological and rheological change between the Jurassic - Lower Eocene limestones and the marly and terrigenous upper sequences (Figures 12c and 12f).

The breakage of the two well separated slip patches (Figure 12d) can be interpreted in terms of along-strike segmentation of the Mirandola ramp. Following Bonini et al. (2014), the carbonate reservoir of the Cavone oilfield is bounded to the east by inherited subvertical faults transverse to the Mirandola thrust-system (Figure 1b). The main transverse fault offsets the top of Mesozoic carbonates ∼5 km to the west of the mainshock epicenter and bounds the eastern shallower slip patch (Figure 12d). Based on this spatial correlation, the transverse fault may reflect a low-strength fractured zone that acted as a barrier for the rupture propagation.

We compared surface coseismic deformation with the geological structures in Figures 12a and 12b. The main displacement lobe matches the Mirandola fold. The geological section crosses a western secondary deformation lobe. The corresponding displacement profile shows an asymmetric curve with a gentler southern slope in which two bumps are recognizable (Figure 12a). This feature reflects the presence of two slip patches, located at different depths: in particular the deeper western patch, with slip peaked at 13 km, could be responsible for the gentle southern flank of the displacement curve. We also hypothesize that the small bumps could be related to the aseismic activation of shallow back-thrusts (Figure 12c).

7.3. Seismotectonic Implications of the Mainshocks Source Models

The obtained rupture models and their relationship with rock lithology and mechanical properties provide key information for a better understanding of the sources of the 2012 mainshocks, whose geometry and seismotectonic interpretation are debated in literature (see Argnani et al., 2016; Bonini et al., 2016; Cheloni et al., 2016).

In previous works, the tectonic style of the Mirandola and Ferrara thrust systems has been interpreted in opposite ways that can be referred to two end-members models. The main thrust faults of each thrust-fold system are imaged as listric structures splaying out from a low-angle basal thrust or, alternatively, as straight, and steeper faults deeply rooted into the basement. In the first model, the steeper portion of the main thrust faults dips at low-angle (in average 28°–35° to SSW) through the Mesozoic carbonates, while the flatter portion splays from a basal detachment (Figure 1c). This major décollement level is located either at the base of the Upper Triassic dolomites at 6–10 km (Livani et al., 2018) to 8–10 km depth (Carminati et al., 2010; Figure 1c), or within the Permian - Middle Triassic basement s.l. at 10–11 km depth (Lavecchia et al., 2015). In the second model, shallow fore- and back-thrusts merge to moderately dipping (∼45°) thrust ramps that cuts through the basement down to mid-crustal depths with nearly straight geometries (Astiz et al., 2014; Juanes et al., 2016).

Bonini et al. (2014) proposed an interpretation close to the first end-member tectonic model where the main thrust faults have flat-ramp (Mirandola structure) or flat-ramp-flat geometries (San Martino and Pilastri structures). In their model, the ramps cut the Mesozoic carbonates with moderate dip-angles of 45°–50° (Mirandola) and 40°–45° (San Martino and Pilastri). Conversely, the Sermide thrust is steeper (55°–65°) and rooted into the basement. In addition, the evolution of the Mirandola ramp was controlled by a Triassic-Jurassic high-angle extensional fault partially reactivated during the Pliocene-Quaternary shortening.

At odds with the aforementioned interpretations, Carannante et al. (2015) and Argnani et al. (2016) maintain that recent-to-current shortening has not been accommodated by the Mirandola and Ferrara thrust systems, rather by Mesozoic extensional faults rooted into the basement, reactivated and inverted after the Middle Pleistocene. These authors ascribed the May 20th and May 29th mainshocks to deep basement faults that steeply dip SSW in the footwall volume of the Mirandola and Pilastri thrust ramps, respectively.

While the geodetic source models of the May 20th mainshock point to the activation of the Middle Ferrara Thrust System (i.e., Pilastri system; Bignami et al., 2012; Cheloni et al., 2016; Pezzo et al., 2013, 2018), the exact association with the causative fault is a matter of debate. The mainshock was alternatively ascribed to either a steep ramp of the Pilastri fault-system (Astiz et al., 2014), the San Martino thrust ramp with slip confined in the Upper Triassic–Lower Jurassic carbonates (Bonini et al., 2014), or a thrust located between the San Martino and Pilastri structures with a hypocentral volume confined along dip within the Upper Triassic dolomites (Lavecchia et al., 2015).

Contrasting interpretations were also proposed for the May 29th mainshock alternatively associated with either the Mirandola ramp defined as an almost planar fault deeply rooted into the basement (Astiz et al., 2014; Juanes et al., 2016), the steeper segment of the Mirandola thrust with slip located in the Mesozoic carbonates (Bonini et al., 2014), the Inner Ferrara Thrust System with an hypocentral volume confined along dip within the Upper Triassic dolomites (Lavecchia et al., 2015). Geodetic models point to the activation of the Mirandola fault-system, but both planar (Pezzo et al., 2018) and listric sources (Cheloni et al., 2016; Pezzo et al., 2013) have been considered.

We definitely show that the May 20th mainshock ruptured the main thrust of the Pilastri thrust-system, as previously hypothesized by some authors (Astiz et al., 2014; Cheloni et al., 2016; Chiarabba et al., 2014; Pizzi & Scisciani, 2012).

We note that the structural settings defined in the shallow part of the "App Orien-1" seismic section is similar to that proposed by Bonini et al. (2014). Unlike our interpretation, these authors ascribed the May 20th mainshock to the San Martino structure. This difference might arise from the aforementioned mislocation of the seismic profile in the ViDEPI database (ViDEPI Project, 2015), and consequently from an accidental, misleading projection of aftershock and mainshock locations onto the geological section. To further corroborate our interpretation, we compare our inversion results with those obtained through a fault that mimics the San Martino's source of Bonini et al. (2014). We repeated a kinematic inversion by adopting a fault plane that is shifted 4 km toward SSW to match the San Martino thrust ramp defined by Bonini et al. (2014) (Figure 5b) and using dip and strike values consistent with those reported by the authors. The comparison of the cost function values shows that our "Pilastri" source provides a significantly better fit for all inverted datasets (see Table S3 in Supporting Information S1).

Regarding the May 29th mainshock, our results point to the rupture of the Mirandola main thrust in agreement with a part of previous works (Astiz et al., 2014; Bonini et al., 2014; Cheloni et al., 2016; Juanes et al., 2016; Pezzo et al., 2018).

Our integrated geological and seismic source models provide, for the first time, evidence of the rupture of moderately dipping (40°–45°) thrust ramps deeply rooted into the basement, within which significant slip occurred during both mainshocks down to 14–16 km depth (Figures 11e and 11f and Figures 12e and 12f). Therefore, our finding reinforces previous interpretations of thrusting along ramps that extend from the upper-crust to mid-crustal depths (Astiz et al., 2014; Juanes et al., 2016).

Very-high Vp and low-Vp/Vs bodies (Vp > 6.5 km/s, Vp/Vs < 1.8) defined by local earthquake tomography at depths >10 km under the Ferrara thrust systems can be ascribed to acid metamorphic Paleozoic rocks of the Hercynian crystalline basement (Chiarabba et al., 2014; Vai, 2001). We therefore reckon that co-seismic slip affected the Mesozoic carbonates and Permo-Triassic basal clastics but also the underlying Hercynian crystalline crust. We speculate that the ruptured ramps could relate to basement faults of the Adria passive paleo-margin inherited from Triassic-Jurassic extensional tectonics and reactivated by compression (Chiarabba et al., 2014; Turrini et al., 2014).

On the contrary, our results disagree with interpretations that the major thrust faults of the Mirandola and Ferrara systems flatten downwards to merge into a basal detachment at depths of 6–10 km (Carminati et al. (2010), see Figure 1c; Livani et al. (2018)) to 10–11 km (Lavecchia et al., 2015). Also, our models conflict with seismotectonic interpretations of the mainshocks with slip confined along dip within the Upper Triassic dolomites (Bonini et al., 2014; Lavecchia et al., 2015).

Our findings are better explained by ramp-dominated, basement-involved thrusting (sensu Butler & Mazzoli, 2006). This deformation style characterizes the late stage of shortening in outer frontal portions of other thrust-and-fold belts (Tavani et al., 2021 and references therein), such as the outer Albanides (Teloni et al., 2021) that presents a sedimentary architecture similar to that of the Adria domain. In the outer Albanides, blind frontal ramps propagating from mid-crustal depths across the crystalline basement and sedimentary cover accommodate on-going deformation, as documented by the 2019, M_w 6.4, Durrës earthquake (Pezzo et al., 2022; Teloni et al., 2021).

In a recent work on the Apennines in central Italy, through the analysis of high-quality background seismicity data De Nardis et al. (2022) provided evidence of two lithospheric-scale active thrusts deepening westward under the Adriatic outer front from upper- to lower-crustal depths. These new data reinforce previous thick-skinned

interpretations of seismic commercial profiles (Coward et al., 1999) and deep-crust reflection data (Lavecchia et al., 2003).

For the northern Apennines, mid-crustal ramps located under the Pedeappenninic thrust front allow modeling recent deformation along the range foothills and have been related to deep, M5+, reverse-faulting earthquakes (Figure 1b) (Fisher et al., 2022; Picotti & Pazzaglia, 2008; Vannoli et al., 2015). Regarding the external buried portion of the thrust belt, Turrini et al. (2014) documents thick-skinned tectonics for the western Po plain where the crystalline basement appears largely involved by thrusting under the Monferrato Arc. Conversely, basement involvement is only supposed for the Emilia and western Ferrara-Romagna arcs. According to these authors, the basement may be involved locally through reactivation of Triassic-Jurassic extensional faults rooted into the crystalline crust, within a predominant thin-skinned style of deformation (i.e., mixed-thin-thick-skinned tectonics).

Across the outer northern Apennines fronts, GPS data documents limited N-S shortening with rates that increase eastwards from <0.5 mm/yr for the Monferrato Arc to 2.5 mm/yr for the eastern Ferrara-Romagna arc (Devoti et al., 2011). Such an increasing trend also characterizes the total seismic moment released by historical and instrumental seismicity (Maesano et al., 2015). In literature (Maesano et al., 2015; and references therein), recent-to-current deformation along the outer Emilia and Ferrara-Romagna fronts is ascribed to blind thrusts cutting the Meso-Cenozoic sedimentary cover. These shallow faults are also considered as primary sources of historical M5+ earthquakes (Vannoli et al., 2015).

The new source models and seismotectonic interpretation of the 2012 mainshocks presented in this study open the possibility that thrust ramps rooted into crystalline basement, as those recognized under the western Po plain (Turrini et al., 2014), play a key role in accommodating shortening along the outer Emilia and western Ferrara-Romagna fronts too. This hypothesis reconciles to some anomalous mid-crustal earthquakes (M_L 4–5) occurred in the Po plain under the Emilia Arc and to the local seismogenic thickness of 20–25 km (Caciagli et al., 2015; Chiarabba & De Gori, 2016; Pondrelli et al., 2006; Scognamiglio et al., 2006).

8. Conclusions

We determined the first source models of the 2012, M_w 6.1 and M_w 6.0, Emilia earthquakes by inverting jointly strong motion and geodetic data. The geometrical parameters of the modeled planar faults honor both subsurface geological models and seismological data (mainshocks/aftershocks hypocenters and focal mechanisms). Unlike previous models relying on either strong motion or geodetic data, the slip distribution for both mainshocks presents two separated asperities and deeper slip patches extending downwards to 14–16 km depth (Figures 11c–11f and Figures 12c–12f).

By integrating the new source models with subsurface geological sections, mainshocks/aftershocks relocations and focal mechanisms, we were able to define a comprehensive seismotectonic interpretation of the 2012 sequence. Our cross-disciplinary survey indicates that the 20th May and 29th May mainshocks ruptured the Pilastri and Mirandola main thrust ramps, respectively, both imaged as moderately dipping faults (45° SSW-ward and 42° S-ward, respectively).

The rupture evolution was controlled by the lithological transition between the Jurassic–Lower Eocene limestone and the Middle Eocene - Miocene sediments that acted as a rheological barrier to propagation of coseismic slip and aftershocks release. Separated asperities might reflect along-strike segmentation of the Mirandola and Middle Ferrara thrust systems due to transverse faults acting as structural barriers.

We argue that the Mirandola and Pilastri folds relate to major thrust ramps rooted into the Paleozoic crystalline basement. Unlike previous interpretations, we unravel that the co-seismic slip was not confined within the Mesozoic carbonates and Permo-Triassic basal clastics but extended under the sedimentary crust into the crystalline basement.

Such a rupture evolution demands ramp-dominated, basement-involved thrusting (sensu Butler & Mazzoli, 2006), differently from published models where both mainshocks activated low-angle thrust faults splaying from relatively shallow basal dècollement 6–10 km (Livani et al., 2018) to 10–11 km deep (Lavecchia et al., 2015).

At a more general scale, our cross-disciplinary investigation underlines once more that combining complete source models (determined by inverting jointly strong-motion and geodetic data) with accurate 3-D aftershocks locations and seismic reflection imaging is mandatory to picture seismic sequences in complex structural settings.

Conflict of Interest

The authors declare no conflicts of interest relevant to this study.

Data Availability Statement

Strong motion data used in this study recorded by the national accelerometric network managed by the Italian Civil Protection are available at https://rischi.protezionecivile.gov.it/en/seismic/activities/emergency-planning-and-damage-scenarios/ran-national-accelerometric-network. Strong motion data recorded by INGV permanent and temporary stations are available from the European Integrated Data Archive (EIDA) at https://eida.ingv.it/en/networks. https://doi.org/10.4401/ag-6152 (for temporary stations). COSMO-SkyMed and Radarsat data, from Pezzo et al., 2013 (https://doi.org/10.1785/0220120171) are available in Data Set S1 and S2 (Supporting Information S1). Raw data from COSMO-SkyMed and Radarsat1 satellites are copyright of the Italian Space Agency of the Canadian Space Agency, respectively. GPS data and high-rate GPS data recorded by four 1 Hz continuous cGPS stations belonging to the RING network are available at http://ring.gm.ingv.it/, Avallone et al. (2012). Seismic reflection sections and well data interpreted in this study are freely available in the ViDEPI database (ViDEPI Project, 2015; https://www.videpi.com/videpi/videpi.asp). Other well data and subsurface structural maps were published in the following papers and reports that are included in the list of references: Astiz et al. (2014), Bencini (2009), Bigi et al. (1991), ISPRA (2015), Juanes et al. (2016), Styles et al. (2014). Most of the figures were made using the GMT software (Wessel & Smith, 1998), and Seismic Analysis Code–SAC (Goldstein & Snoke, 2005).

Acknowledgments
Comments by the Editor Rachel Abercrombie, the Associate Editor and two anonymous reviewers helped to improve the manuscript and are thankfully acknowledged. L.I. thanks Dr. F. Maesano of the INGV that provided geographical coordinates of the seismic profile "App Orien-1" and for fruitful discussions on the Po plain subsurface structure. We thank Dr. V. Convertito, and Dr. A. Ganas for sharing results of his investigations. We also thank Dr. A. Avallone and Dr. D. Piccinini for fruitful discussions.

References

Argnani, A., Carannante, S., Massa, M., Lovati, S., & D'Alema, M. (2016). Reply to the "Comment on "The May 1 20 (M_W 6.1) and 29 (M_W 6.0), 2012, Emilia (Po Plain, northern Italy) earthquakes: New seismotectonic implications from subsurface geology and high-quality hypocenter location" by Carannante et al., 2015" by Bonini L., et al. *Tectonophysics*, *693*, 157–162. https://doi.org/10.1016/j.tecto.2016.10.006

Astiz, L., Dieterich, J. H., Frohlich, C., Hager, B. H., Juanes, R., & Shaw, J. H. (2014). On the potential for induced seismicity at the Cavone oilfield: Analysis of geological and geophysical data, and geomechanical modeling. Report for the Laboratorio di Monitoraggio Cavone. Retrieved from http://labcavone.it/documenti/32/allegatrapporto-studiogiacimento.pdf

Avallone, A., D'Anastasio, E., Serpelloni, E., Latorre, D., Cavaliere, A., D'Ambrosio, C., et al. (2012). High-rate (1 Hz to 20 Hz) GPS coseismic dynamic displacements carried out during the Emilia 2012 seismic sequence. *Annals of Geophysics*, *55*, 4. https://doi.org/10.4401/ag-6162

Bencini, R. (2009). Studio multidisciplinare del sottosuolo dell'area di Rivara (Modena, Italy). In *Rivara gas storage Project*. https://doi.org/10.13140/RG.2.1.1548.6328

Bigi, S., Cosentino, D., Parotto, M., Sartori, R., & Scandone, P. (1991). Structural model of Italy, scale 1:500.000, C. N. R. *Progetto Finalizzato Geodinamica*. In *Quad. Ric. Sci., N. 114* (Vol. 3). Selca.

Bignami, C., Burrato, P., Cannelli, V., Chini, M., Falcucci, E., Ferretti, A., et al. (2012). Coseismic deformation pattern of the Emilia 2012 seismic sequence imaged by Radarsat-1 interferometry. *Annales Geophysicae*, *55*(4), 789–793. https://doi.org/10.4401/ag-6157

Bonini, L., Toscani, G., & Seno, S. (2014). Three-dimensional segmentation and different rupture behaviour during the 2012 Emilia seismic sequence (Northern Italy). *Tectonophysics*, *630*, 33–42. https://doi.org/10.1016/j.tecto.2014.95.006

Bonini, L., Toscani, G., & Seno, S. (2016). Comment on "The May 20 (M_W 6.1) and 29 (M_W 6.0), 2012, Emilia (Po Plain, Northern Italy) earthquakes: New seismotectonic implications from subsurface geology and high-quality hypocenter location" by Carannante et al., 2015. *Tectonophysics*, *688*, 182–188. https://doi.org/10.1016/j.tecto.2016.02.001

Bordoni, P., Azzara, R. M., Cara, F., Cogliano, R., Cultrera, G., Di Giulio, G., et al. (2012). Preliminary results from EMERSITO, the rapid response network for site effect studies. *Annales Geophysicae*, *55*(4), 599–607. https://doi.org/10.4401/ag-6153

Burrato, P., Ciucci, F., & Valensise, G. (2003). An inventory of river anomalies in the Po plain, Northern Italy: Evidence for active blind thrust faulting. *Annales Geophysicae*, *46*(5), 865–882.

Butler, R. W. H., & Mazzoli, S. (2006). Styles of continental contraction: A review and introduction. In S. Mazzoli & R. W. H. Butler (Eds.), *Styles of continental contraction* (Vol. 414, pp. 1–10). Geological Society of America. https://doi.org/10.1130/2006.2414(01)

Caciagli, M., Camassi, R., Danesi, S., Pondrelli, S., & Salimbeni, S. (2015). Can we consider the 1951 Caviaga (northern Italy) earthquakes as non induced events? *Seismological Research Letters*, *86*, 5–1344. https://doi.org/10.1785/0220150001

Carannante, S., Argnani, A., Massa, M., D'Alema, E., Lovati, S., Moretti, M., et al. (2015). The May 20 (M_w 6.1) and 29 (M_w 6.0) 2012, Emilia (Po Plain, Northern Italy) earthquakes: New seismotectonic implications from subsurface geology and high-quality hypocenter location. *Tectonophysics*, *655*, 107–123. https://doi.org/10.1016/j.tecto.2015.05.015

Carminati, E., & Martinelli, G. (2002). Subsidence rates in the Po plain (northern Italy): The relative impact of natural and anthropogenic causation. *Engineering Geology*, *66*(3–4), 241–255. https://doi.org/10.1016/S0013-7952(02)00031-5

Carminati, E., Scrocca, D., & Doglioni, C. (2010). Compaction-induced stress variations with depth in an active anticline: Northern Apennines. *Journal of Geophysical Research*, *115*(B2), B02401. https://doi.org/10.1029/2009JB006395

Causse, M., Cultrera, G., Moreau, L., Herrero, A., Schiappapietra, E., & Courboulex, F. (2017). Bayesian rupture imaging in a complex medium: The 29 May 2012 Emilia, Northern Italy, earthquake. *Geophysical Research Letters*, *44*(15), 7783–7792. https://doi.org/10.1002/2017GL074698

Cesca, S., Braun, T., Maccaferri, F., Passatelli, L., Rivalta, E., & Dahm, T. (2013). Source modelling of the M5–6 Emilia-Romagna, Italy, earthquakes (2012 May 20–29). *Geophysical Journal International*, *193*(3), 1658–1672. https://doi.org/10.1093/gji/ggt069

Cheloni, D., Giuliani, R., D'Agostino, N., Mattone, M., Bonano, M., Fornaro, G., et al. (2016). New insights into fault activation and stress transfer between en echelon thrusts: The 2012 Emilia, northern Italy, earthquake sequence. *Journal of Geophysical Research: Solid Earth*, *121*(6), 4742–4766. https://doi.org/10.1002/2016JB012823

Chiarabba, C., & De Gori, P. (2016). The seismogenic thickness in Italy: Constraints on potential magnitude and seismic hazard. *Terra Nova*, *28*(6), 402–408. https://doi.org/10.1111/ter.12233

Chiarabba, C., De Gori, P., Improta, L., Lucente, F. P., Moretti, M., Govoni, A., et al. (2014). Frontal compression along the Apennines thrust system: The Emilia 2012 example from seismicity to crustal structure. *Journal of Geodynamics*, *82*, 98–109. https://doi.org/10.1016/j.jog.2014.09.003

Cirella, A., Piatanesi, A., Tinti, E., Chini, M., & Cocco, M. (2012). Complexity of the rupture process during the 2009 L'Aquila, Italy, earthquake. *Geophysical Journal International*, *190*(1), 607–621. https://doi.org/10.1111/j.1365-246x.2012.05505.x

Convertito, V., Pino, N. A., & Piccinini, D. (2021). Concentrated slip and low rupture velocity for the May 20, 2012, M_w 5.8, Po Plain (Northern Italy) earthquake revealed from the analysis of source time functions. *Journal of Geophysical Research: Solid Earth*, *126*(1), e2019JB019154. https://doi.org/10.1029/2019JB019154

Coward, M. P., De Donatis, M., Mazzoli, S., Paltrinieri, W., & Wezel, F. C. (1999). Frontal part of the northern Apennines fold and thrust belt in the Romagna-Marche area (Italy): Shallow and deep structural styles. *Tectonics*, *18*(3), 559–574. https://doi.org/10.1029/1999tc900003

De Nardis, R., Pandolfi, C., Cattaneo, M., Monachesi, G., Cirillo, D., Ferrarini, F., et al. (2022). Lithospheric double shear zone unveiled by microseismicity in a region of slow deformation. *Scientific Reports*, *12*(1), 21066. https://doi.org/10.1038/s41598-022-24903-1

Devoti, R., Esposito, A., Pietrantonio, G., Pisani, A. R., & Riguzzi, F. (2011). Evidence of large scale deformation patterns from GPS data in the Italian subduction boundary. *Earth and Planetary Science Letters*, *311*(3–4), 230–241. https://doi.org/10.1016/j.epsl.2011.09.034

Doglioni, C., Harabaglia, P., Merlini, S., Mongelli, F., Peccerillo, A., & Piromallo, C. (1999). Orogens and slab vs. their direction of subduction. *Earth-Science Reviews*, *45*(3–4), 167–208. https://doi.org/10.1016/S0012-8252(98)00045-2

Fantoni, R., & Franciosi, R. (2010). Tectono-sedimentary setting of the Po Plain and Adriatic foreland. *Rend. Fis. Acc. Lincei*, *21*(S1), S197–S209. https://doi.org/10.1007/s12210-010-0102-4

Fisher, J. A., Pazzaglia, F. J., Anastasio, D. J., & Gallen, S. F. (2022). Linear inversion of fluvial topography in the northern Apennines: Comparison of base-level fall to crustal shortening. *Tectonics*, *41*(11), e2022TC007379. https://doi.org/10.1029/2022TC007379

Gallovič, F., Imperatori, W., & Mai, P. M. (2015). Effects of three-dimensional crustal structure and smoothing constraint on earthquake slip inversions: Case study of the M_w6.3 2009 L'Aquila earthquake. *Journal of Geophysical Research*, *120*(1), 428–449. https://doi.org/10.1002/2014JB011650

Ganas, A., Roumelioti, Z., & Chousianitis, K. (2012). Static stress transfer from the May 20, 2012, M 6.1 Emilia-Romagna (northern Italy) earthquake using a co-seismic slip distribution model. *Annals of Geophysics*, *55*(4). https://doi.org/10.4401/ag-6176

Goldstein, P., & Snoke, A. (2005). SAC availability for the IRIS community, incorporated institutions for seismology data management center electronic newsletter.

Govoni, A., Marchetti, A., De Gori, P., Di Bona, M., Lucente, F. P., Improta, L., et al. (2014). The 2012 Emilia seismic sequence (northern Italy): Imaging the thrust fault system by accurate aftershock location. *Tectonophysics*, *622*, 44–55. https://doi.org/10.1016/j.tecto.2014.02.013

ISPRA. (2015). Modello geologico 3D e geopotenziali della Pianura Padana Centrale (Progetto GeoMol). *Report ISPRA*, *234/2015*, 104. Retrieved from https://www.isprambiente.gov.it/files/pubblicazioni/rapporti/R_234_15.pdf

Juanes, R., Jha, B., Hager, B. H., Shaw, J. H., Plesch, A., Astiz, L., et al. (2016). Were the May 2012 Emilia-Romagna earthquakes induced? A coupled flow-geomechanics modeling assessment. *Geophysical Research Letters*, *43*(13), 6891–6897. https://doi.org/10.1002/2016GL069284

Lavecchia, G., Boncio, P., & Creati, N. (2003). A lithospheric-scale seismogenic thrust in central Italy. *Journal of Geodynamics*, *36*(1–2), 79–94. https://doi.org/10.1016/s0264-3707(03)00040-1

Lavecchia, G., De Nardis, R., Costa, G., Tiberi, L., Ferrarini, F., Cirillo, D., et al. (2015). Was the Mirandola thrust really involved in the Emilia 2012 seismic sequence (northern Italy)? Implications on the likelihood of triggered seismicity effects. *Bollettino di Geofisica Teorica ed Applicata*, *56*, 461–488.

Livani, M., Scrocca, D., Arecco, P., & Doglioni, C. (2018). Structural and stratigraphic control on salient and recess development along a thrust belt front: The Northern Apennines (Po Plain, Italy). *Journal of Geophysical Research: Solid Earth*, *123*(5), 4360–4387. https://doi.org/10.1002/2017JB015235

Lomax, A., Virieux, J., Volant, P., & Berge, C. (2000). Probabilistic earthquake location in 3D and layered models: Introduction of a Metropolis-Gibbs method and comparison with linear locations. In C. H. Thurber & N. Rabinowitz (Eds.), *Advances in seismic event location* (pp. 101–134).

Maesano, F. E., D'Ambrogi, C., Burrato, P., & Toscani, G. (2015). Slip-rates of blind thrusts in slow deforming areas: Examples from the Po Plain (Italy). *Tectonophysics*, *643*, 8–25. https://doi.org/10.1016/j.tecto.2014.12.007

Malagnini, L., Herrmann, R. B., Munafo, I., Buttinelli, M., Anselmi, M., Akinci, A., & Boschi, B. (2012). The 2012 Ferrara seismic sequence: Regional crustal structure, earthquake sources, and seismic hazard. *Geophysical Research Letters*, *39*(19), L19302. https://doi.org/10.1029/2012GL053214

Mariotti, G., & Doglioni, C. (2000). The dip of the foreland monocline in the Alps and Apennines. *Earth and Planetary Science Letters*, *181*(1–2), 191–202. https://doi.org/10.1016/S0012-821X(00)00192-8

Marzorati, S., Carannante, S., Cattaneo, M., D'Alema, E., Frapiccini, M., Ladina, C., et al. (2012). Automated control procedures and first results from the temporary seismic monitoring of the 2012 Emilia sequence. *Annals of Geophysics*, *55*, 4. https://doi.org/10.4401/ag-6116

Milana, G., Bordoni, P., Cara, F., Di Giulio, G., Hailemikael, S., & Rovelli, A. (2014). 1D velocity structure of the Po River plain (Northern Italy) assessed by combining strong motion and ambient noise data. *Bulletin of Earthquake Engineering*, *12*(5), 2195–2209. https://doi.org/10.1007/s10518-013-9483-y

Molinari, I., Argnani, A., Morelli, A., & Basini, P. (2015). Development and testing of a 3D seismic velocity model of the Po Plain sedimentary basin, Italy. *Bulletin of the Seismological Society of America*, *105*(2a), 753–764. https://doi.org/10.1785/0120140204

Montone, P., Mariucci, M. T., Pondrelli, S., & Amato, A. (2004). An improved stress map for Italy and surrounding regions (central Mediterranean). *Journal of Geophysical Research*, *109*(B10), B10410. https://doi.org/10.1029/2003JB002703

Moretti, M., Abruzzese, L., Zeid, N. A., Augliera, P., Azzara, R. A., Barnaba, C., et al. (2012). Rapid-response to the earthquake emergency of May 2012, in the Po Plain, northern Italy. *Annales Geophysicae*, *55*(4), 583–590. https://doi.org/10.4401/ag-6152

Nardon, S., Marzorati, D., Bernasconi, A., Cornini, S., Gonfalini, M., Mosconi, S., et al. (1991). Fractured carbonate reservoir characterization and modeling a multidisciplinary case study from the Cavone oil field, Italy. *First Break*, *9*(12), 553–565.

Nespoli, M., Belardinelli, M. E., Anderlini, L., Bonafede, M., Pezzo, G., Todesco, M., & Rinald, A. P. (2017). Effects of layered crust on the coseismic slip inversion and related CFF variations: Hints from the 2012 Emilia Romagna earthquake. *Physics of the Earth and Planetary Interiors*, *273*, 23–35. https://doi.org/10.1016/j.pepi.2017.10.011

Patacca, E., Scandone, P., Di Luzio, E., Cavinato, G. P., & Parotto, M. (2008). Structural architecture of the central Apennines: Interpretation of the CROP 11 seismic profile from the Adriatic coast to the orographic divide. *Tectonics*, *27*(3), 1–36. https://doi.org/10.1029/2005TC001917

Pezzo, G., De Gori, P., Lucente, F. P., & Chiarabba, C. (2018). Pore pressure pulse drove the 2012 Emilia (Italy) series of earthquakes. *Geophysical Research Letters*, *45*(2), 682–690. https://doi.org/10.1002/2017GL076110

Pezzo, G., Merryman, J. P., Boncori, P., Tolomei, C., Salvi, S., Atzori, S., et al. (2013). Coseismic deformation and source modeling of the May 2012 Emilia (Northern Italy), earthquakes. *Seismological Research Letters*, *84*(4), 645–655. https://doi.org/10.1785/0220120171

Pezzo, G., Palano, M., & Chiarabba, C. (2022). Rotation at subduction margins: How complexity at fault-scale (the 2019 Albanian M_w 6.4 earthquake) mirrors the regional deformation. *Terra Nova*, *34*(3), 244–252. https://doi.org/10.1111/ter.12584

Piatanesi, A., Cirella, A., Spudich, P., & Cocco, M. (2007). A global search inversion for earthquake kinematic rupture history: Application to the 2000 western Tottori, Japan earthquake. *Journal of Geophysical Research*, *112*(B7), B07314. https://doi.org/10.1029/2006JB004821

Piccinini, D., Pino, N. A., & Saccorotti, G. (2012). Source complexity of the May 20, 2012 M_w 5.9, Ferrara (Italy) event. *Annales Geophysicae*, *55*, 568–573.

Picotti, V., & Pazzaglia, F. J. (2008). A new active tectonic model for the construction of the Northern Apennines mountain front near Bologna (Italy). *Journal of Geophysical Research*, *113*(B8), B08412. https://doi.org/10.1029/2007JB005307

Pieri, M., & Groppi, G. (1981). *Subsurface geological structure of the Po Plain, Italy* (Vol. 414, pp. 1–13). C. N. R. Progetto Finalizzato Geodinamica.

Pizzi, A., & Scisciani, V. (2012). The May 2012 Emilia (Italy) earthquakes: Preliminary interpretations on the seismogenic source and the origin of the coseismic ground effects. *Annales Geophysicae*, *55*(4), 751–757. https://doi.org/10.4401/ag-6171

Pondrelli, S., Salimbeni, S., Ekstrom, G., Morelli, A., Gasperini, P., & Vannucci, G. (2006). The Italian CMT dataset from 1977 to the present. *Physics of the Earth and Planetary Interiors*, *159*(3–4), 286–303. https://doi.org/10.1016/j.pepi.2006.07.008

Pondrelli, S., Salimbeni, S., Perfetti, P., & Danecek, P. (2012). Quick regional centroid moment tensor solutions for the Emilia 2012 (northern Italy) seismic sequence. *Annales Geophysicae*, *55*(4). https://doi.org/10.4401/ag-6146

Rovida, A., Camassi, R., Gasperini, P., & Stucchi, M. (2011). CPTI11, the 2011 version of the parametric catalogue of Italian earthquakes. https://doi.org/10.6092/INGV.IT-CPTI11

Royden, L. H., Patacca, E., & Scandone, P. (1987). Segmentation and configuration of subducted lithosphere in Italy: An important control on thrust-belt and foredeep-basin evolution. *Geology*, *15*(8), 714–717. https://doi.org/10.1130/0091-7613(1987)15<714:sacosl>2.0.co;2

Salvi, S., Tolomei, C., Merrymar, J. P., Pezzo, G., Atzori, S., Antonioli, A., et al. (2012). Activation of the SIGRIS monitoring system for ground deformation mapping during the Emilia 2012 seismic sequence using COSMO-SkyMed InSAR data. *Annals of Geophysics*, *55*, 4. https://doi.org/10.4401/ag-6181

Saraò, A., & Peruzza, L. (2012). Fault-plane solutions from moment-tensor inversion and preliminary Coulomb stress analysis for the Emilia Plain. *Annals of Geophysics*, *55*, 4. https://doi.org/10.4401/ag-6134

Scognamiglio, L., Margheriti, L., Mele, F. M., Tinti, E., Bono, A., De Gori, P., et al. (2012). The 2012 Pianura Padana Emiliana seismic sequence: Locations, moment tensors and magnitudes. *Annales Geophysicae*, *55*, 549–559.

Scognamiglio, L., Magnoni, F., Tinti, E., & Casarotti, E. (2016). Uncertainty estimations for moment tensor inversions: The issue of the 2012 May 20 Emilia earthquake. *Geophysical Journal International*, *206*(2), 792–806. https://doi.org/10.1093/gji/ggw173

Scognamiglio, L., Tinti, E., & Quintiliani, M. (2006). Time domain moment tensor (TDMT) [Dataset]. Istituto Nazionale di Geofisica e Vulcanologia (INGV). https://doi.org/10.13127/TDMT.11

Selvaggi, G., Ferulano, F., Di Bona, M., Frepoli, A., Azzara, R., Basili, A., et al. (2001). The M_w 5.4 Reggio Emilia 1996 earthquake: Active compressional tectonics in the Po Plain, Italy. *Geophysical Journal International*, *144*, 1–13. https://doi.org/10.1046/j.0956-540X.2000.01255.x

Serpelloni, E., Anderlini, L., Avallone, A., Cannelli, V., Cavaliere, A., Cheloni, D., et al. (2012). GPS observations of coseismic deformation following the May 20th and 29, 2012, Emilia seismic events (northern Italy): Data, analysis and preliminary models. *Annales Geophysicae*, *55*(4), 759–766. https://doi.org/10.4401/ag-6168

Styles, P., Gasparini, P., Huenges, E., Scandone, P., Lasocki, S., & Terlizzese, F. (2014). Report on the hydrocarbon exploration and seismicity in Emilia region (ICHESE report). Retrieved from http://mappegis.regione.emilia-romagna.it/gstatico/documenti/ICHESE/ICHESE_Report.pdf

Tavani, S., Granado, P., Corradetti, A., Camanni, G., Vignaroli, G., Manatschal, G., et al. (2021). Rift inheritance controls the switch from thin- to thick-skinned thrusting and basal décollement re-localization at the subduction-to-collision transition. *GSA Bulletin*, *133*(9–10), 2157–2170. https://doi.org/10.1130/B35800.1

Teloni, S., Invernizzi, C., Mazzoli, S., Pierantoni, P. P., & Spina, V. (2021). Seismogenic fault system of the M_w 6.4 November 2019 Albania earthquake: New insights into the structural architecture and active tectonic setting of the outer Albanides. *Journal of the Geological Society, London*, *178*(2), 193. https://doi.org/10.1144/jgs2020-193

Tinti, E., Fukuyama, E., Piatanesi, A., & Cocco, M. (2005). A kinematic source time function compatible with earthquake dynamics. *Bulletin of the Seismological Society of America*, *95*(4), 1211–1223. https://doi.org/10.1785/0120040177

Turrini, C., Lacombe, O., & Roure, F. (2014). Present-day 3D structural architecture of the Pô Valley basin, northern Italy. *Marine and Petroleum Geology*, *56*, 266–289. https://doi.org/10.1016/j.marpetgeo.2014.02.006

Vai, G. B. (2001). Basement and early (pre-Alpine) history. In G. B. Vai & I. P. Martini (Eds.), *Anatomy of an Orogen: The apennines and adjacent mediterranean basins* (pp. 121–150). Kluwer Acad.

Vannoli, P., Burrato, P., & Valensise, G. (2015). The seismotectonics of the Po Plain (northern Italy): Tectonic diversity in a blind faulting domain. *Pure and Applied Geophysics*, *172*(5), 1105–1142. https://doi.org/10.1007/s00024-014-0873-0

ViDEPI Project. (2015). *Visibility of petroleum exploration data in Italy*. Ministry of Economic Development. National Mining Office for Hydrocarbons and Earth Resources - UNMIG. Well data and seismic reflection profiles Retrieved from http://unmig.sviluppoeconomico.gov.it/videpi/videpi.asp

Wessel, P., & Smith, W. H. F. (1998). New, improved version of the generic mapping tools released. *EOS Transactions American Geophysical Union*, *79*(47), 579. https://doi.org/10.1029/98EO00426

References From the Supporting Information

Brocher, T. M. (2005). Empirical relations between elastic wavespeeds and density in the Earth's crust. *Bulletin of the Seismological Society of America*, *95*(6), 2081–2092. https://doi.org/10.1785/0120050077

Brocher, T. M. (2008). Compressional and shear-wave velocity versus depth relations for common rock types in northern California. *Bulletin of the Seismological Society of America*, *98*(2), 950–968. https://doi.org/10.1785/0120060403

Graves, R. W., & Wald, D. J. (2001). Resolution analysis of finite source inversion using one- and three-dimensional Green's functions: 1. Strong motions. *Journal of Geophysical Research*, *106*(B5), 8745–8766. https://doi.org/10.1029/2000jb900436

Hok, S., & Fukuyama, E. (2010). A new BIEM for rupture dynamics in half-space and its application to the 2008 Iwate-Miyagi Nairiku earthquake. *Geophysical Journal International*, *184*(1), 301–324. https://doi.org/10.1111/j.1365-246X.2010.04835.x

Ide, S., & Takeo, M. (1997). Determination of constitutive relations of fault slip based on seismic wave analysis. *Journal of Geophysical Research*, *102*(B12), 27379–27391. https://doi.org/10.1029/97jb02675

Pulido, N., & Dalguer, L. (2009). Estimation of the high-frequency radiation of the 2000 Tottori (Japan) earthquake based on a dynamic model of fault rupture: Application to the strong ground motion simulation. *Bulletin of the Seismological Society of America*, *99*(4), 2305–2322. https://doi.org/10.1785/0120080165

Shibutani, T., Sambridge, M., & Kennett, B. (1996). Genetic algorithm inversion for receiver functions with application to crust and uppermost mantle structure beneath Eastern Australia. *Geophysical Research Letters*, *23*(14), 1829–1832. https://doi.org/10.1029/96gl01671

Vallée, M., Charléty, J., Ferreira, A., Delouis, M. G., & Vergoz, J. (2011). SCARDEC: A new technique for the rapid determination of seismic moment magnitude, focal mechanism and source time functions for large earthquakes using body wave deconvolution. *Geophysical Journal International*, *184*(1), 338–358. https://doi.org/10.1111/j.1365-246x.2010.04836.x